OPEN

Light: Science & Applications (2018) 7, 17138; doi:10.1038/lsa.2017.138
Official journal of the CIOMP 2047-7538/18
www.nature.com/lsa

ARTICLE

Monolithically integrated stretchable photonics

Lan Li[1,*], Hongtao Lin[1,*], Shutao Qiao[2,*], Yi-Zhong Huang[1,3], Jun-Ying Li[1,4], Jérôme Michon[1], Tian Gu[1], Carlos Alosno-Ramos[5], Laurent Vivien[5], Anupama Yadav[6], Kathleen Richardson[6], Nanshu Lu[2] and Juejun Hu[1]

Mechanically stretchable photonics provides a new geometric degree of freedom for photonic system design and foresees applications ranging from artificial skins to soft wearable electronics. Here we describe the design and experimental realization of the first single-mode stretchable photonic devices. These devices, made of chalcogenide glass and epoxy polymer materials, are monolithically integrated on elastomer substrates. To impart mechanical stretching capability to devices built using these intrinsically brittle materials, our design strategy involves local substrate stiffening to minimize shape deformation of critical photonic components, and interconnecting optical waveguides assuming a meandering Euler spiral geometry to mitigate radiative optical loss. Devices fabricated following such design can sustain 41% nominal tensile strain and 3000 stretching cycles without measurable degradation in optical performance. In addition, we present a rigorous analytical model to quantitatively predict stress-optical coupling behavior in waveguide devices of arbitrary geometry without using a single fitting parameter.
Light: Science & Applications (2018) **7,** 17138; doi:10.1038/lsa.2017.138; published online 9 February 2018

Keywords: chalcogenide glass; integrated photonics; optical resonator; strain-optical coupling; stretchable photonics

INTRODUCTION

In recent years, the increasing penetration of flexible devices into the consumer products market has led to a surge of interest in mechanically flexible photonics[1,2]. In addition to being an essential component in consumer electronics, flexible photonics is now enabling a plethora of emerging applications including board-level optical interconnects[3–8], optomechanical tuning[9–11], epidermal monitoring[12], strain sensing[13], and conformal photonics[14,15]. While our earlier work has led to foldable photonic devices with record optical performance and extraordinary mechanical ruggedness[16–18], it is often mandated in these applications that the devices are not only bendable, but also stretchable. For instance, human skin is a soft elastic material with up to 20% stretchability and perfect reversibility[19], which demands epidermal devices to exhibit commensurate deformation capability. Stretching capability is also indispensable for wrinkle-free conformal integration on curvilinear surfaces. Previously reported stretchable integrated photonics have been entirely made of elastomer materials[20,21], which severely limits the available material options. Furthermore, the elastomer waveguides are heavily multimode, which poses a major constraint for many applications. While hybrid transfer based techniques can be applied to produce stretchable structures comprising isolated dielectric nanorods embedded inside an elastomer matrix[22–24], this particular geometry is incompatible with most integrated photonic devices.

In this paper, we present the design and the first experimental demonstration of single-mode stretchable integrated photonic devices fabricated using chalcogenide glass (ChG) and epoxy polymer. Our material selections allow photonic components with both high and low index contrasts to be seamlessly integrated in the same device platform. This unique feature combines the best of both worlds: for example, we can take advantage of the reduced propagation loss in low-index-contrast optics while leveraging high-index-contrast (HIC) elements to attain tight optical confinement and superior diffraction efficiency. The material choices further enable monolithic photonic integration on elastomeric substrates, formerly considered a challenging task due to the gigantic coefficient of thermal expansion (CTE) of elastomers[25–28], which is one to two orders of magnitude larger than those of inorganic semiconductor and dielectric materials.

Both the glass and epoxy polymer, however, are intrinsically brittle. To impart mechanical stretchability to devices made of these materials, we have developed a mechanical design where functional optical components are located on isolated stiff 'islands' and interconnected through optical waveguides with a serpentine shape. Local substrate stiffening at the islands suppresses strain exerted on the optical components[29]. Analogous to helical springs, the serpentine waveguide geometry can accommodate large elongation without fracture. We note that while similar meandering metal wire designs have already been well formulated in the context of stretchable electronic

[1]Department of Materials Science & Engineering, Massachusetts Institute of Technology, Cambridge, Massachusetts, USA; [2]Department of Aerospace Engineering and Engineering Mechanics, University of Texas at Austin, Austin, Texas, USA; [3]Department of Electronic Engineering, Xiamen University, Xiamen, China; [4]Key Laboratory of Optoelectronic Technology & System, Education Ministry of China, College of Opto-Electronic Engineering, Chongqing University, Chongqing, China; [5]Centre for Nanoscience and Nanotechnology, CNRS, Univ. Paris-Sud, Universite Paris-Saclay, Orsay, C2N—Orsay, France and [6]The College of Optics & Photonics, University of Central Florida, Orlando, Florida, USA
*These authors contributed equally to this work.
Correspondence: L Li, Email: lanli1@mit.edu; J Hu, Email: hujuejun@mit.edu
Received 15 June 2017; revised 6 October 2017; accepted 6 October 2017; accepted article preview online 10 October 2017
The accepted article preview was available with the details: *Light: Science & Applications* (2018) 7, e17138; doi: 10.1038/lsa.2017.138

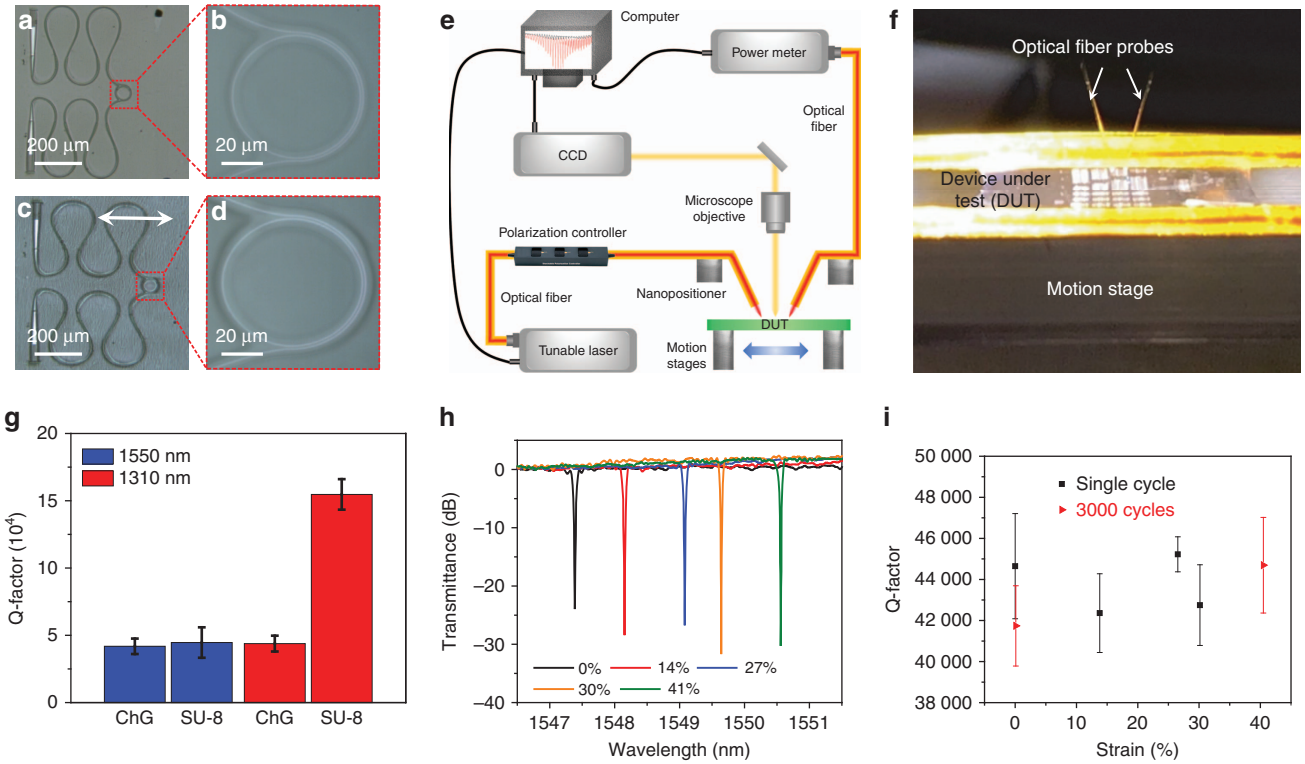

Figure 1 (**a**–**d**) Top-view micrographs of a stretchable device (**a**, **b**) in its undeformed state and (**c**, **d**) at 36% nominal tensile strain; the arrow in **c** indicates the stretching direction; (**e**) schematic diagram of the experimental characterization setup; (**f**) a photo of a stretched device under test; (**g**) measured TE-polarization Q-factors of ChG/SU-8 (labeled as 'ChG') and SU-8/PDMS (labeled as 'SU-8') resonator devices at 1310 and 1550 nm wavelengths; (**h**) normalized optical transmittance spectra of a ChG/SU-8 stretchable resonator at different nominal strain levels; (**i**) Q-factors of ChG/SU-8 resonator devices before and after 3000 stretching cycles at 41% nominal strain. The error bars indicate standard deviations of resonant peaks between the wavelength ranges of 1540–1570 nm. DUT, device under test.

circuits[30–33], such layouts have to be judiciously re-engineered to mitigate excessive radiative optical losses when adapted to integrated optical waveguides.

These mechanical design principles are experimentally implemented to realize highly stretchable photonic circuits and quantitatively validated through finite element mechanical models coupled with a rigorous strain-optical coupling theory. Unlike previously formulated strain-optical coupling analyses which either apply only to limited cases of specific waveguide geometries[34,35] or involve parameters that cannot be straightforwardly evaluated and hence are descriptive in nature[13], our new approach enables quantitative prediction of strain-induced drift of device optical characteristics without a single fitting parameter.

The design rationale, theoretical framework and integration routes outlined above are elaborated in the following sections. They are also generically applicable to mechanically flexible optical systems made from a wide cross-section of materials to meet diverse needs in various application scenarios.

MATERIALS AND METHODS

Stretchable device fabrication

Device fabrication was performed at the MIT Microsystems Technology Laboratories and the Harvard Center for Nanoscale Systems. The handler substrates are bare silicon wafers cleaved into 1' by 1' square pieces (Silicon Quest International). The following layers were then sequentially coated on the handler substrates: polydimethylsiloxane (PDMS) (3 μm thick, Dow Corning Sylgard 184 elastomer with a 10:1 monomer/curing agent mixing ratio and diluted in hexane), SU-8 (0.8 μm thick, Microchem SU-8 2000.5), and $Ge_{23}Sb_7S_{70}$ glass (450 nm thick). The PDMS and SU-8 layers were formed via spin coating. Prior to PDMS coating, the substrates were silanized to facilitate structure delamination upon completion of fabrication. The substrates were also briefly treated in oxygen plasma before SU-8 coating to promote layer adhesion. The $Ge_{23}Sb_7S_{70}$ glass film was deposited via thermal evaporation using a custom-designed system (PVD Products, Inc.), during which the substrate was held near room temperature[36,37]. The deposition rate was monitored in real-time using a quartz crystal microbalance and was stabilized at 20Å s^{-1}. The glass film was subsequently patterned on an Elionix ELS-F125 electron beam lithography system using Microchem SU-8 2000.2 as the electron beam resist followed by fluorine plasma etching[38]. The etched glass photonic devices were encapsulated in a second laminate of SU-8 epoxy (Microchem SU-8 2002), which also serves as an electron beam resist and an etch mask to define the serpentine structures in the SU-8 layers. Finally, a second PDMS layer of about 100 μm in thickness (10:1 monomer/curing agent mixing ratio and without hexane dilution) was spin coated and the entire structure was delaminated from the handler using a water-soluble tape (WST-1, kaptontape.com), which was later removed by rinsing in diluted HCl solution. The fabricated devices were flood exposed under a halogen lamp before optical testing to nullify the glass film's photosensitivity.

Calibration sample fabrication

A 2.8-μm-thick SU-8 film (Microchem SU-8 2002) was first coated on a hander silicon wafer with 300-nm thermal oxide (Silicon Quest International). A 450-nm-thick $Ge_{23}Sb_7S_{70}$ glass film was then

doi:10.1038/lsa.2017.138

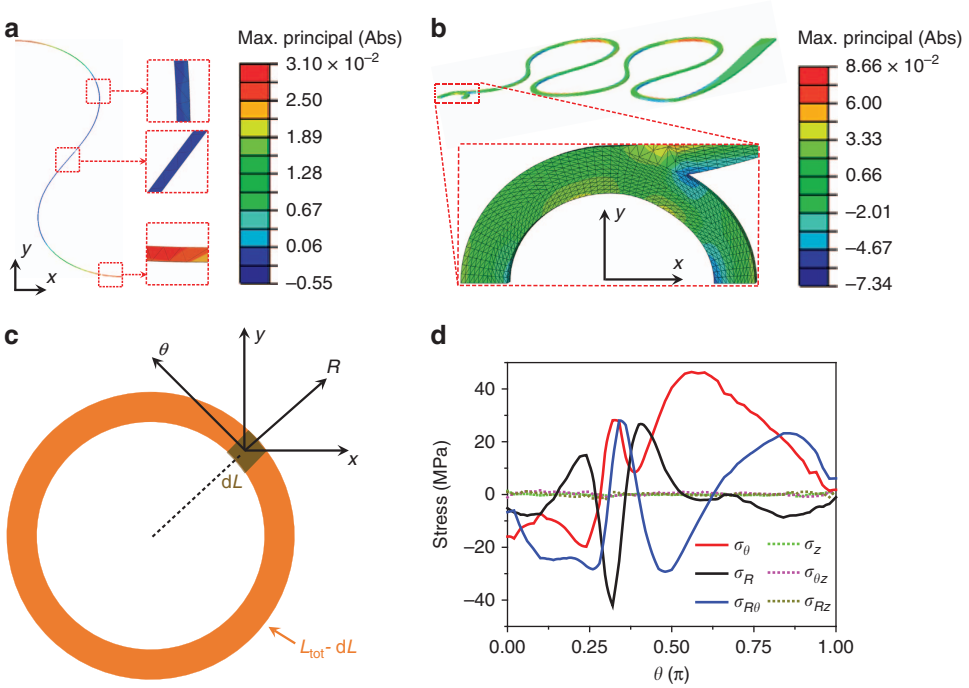

Figure 2 Micro-mechanical FEM simulations: (**a**) strain distribution in an Euler-spiral-shaped ChG waveguide: the insets plot the strain profiles at high-symmetry points of the Euler spiral structure; (**b**) strain field in the stretchable device structure shown in Figure 1a; (**c**) schematic top-view layout of a ChG micro-ring resonator; (**d**) stress components along the azimuth of a ChG micro-ring resonator in the stretchable device structure of Figure 1a. The strain components are defined with respect to the coordinate systems illustrated in **c** and *z* is the out-of-plane direction. All the simulation results correspond to the case of 41% nominal tensile strain. Max., maximum.

thermally evaporated onto the substrate. Fabry-Perot cavities were subsequently patterned using electron beam lithography and capped with another 40-μm-thick SU-8 epoxy layer (Microchem SU-8 2025) before delaminated from the handler substrate using a Kapton tape to form freestanding, bendable membranes[16].

Device characterization

Figure 1e schematically illustrates the optomechanical measurement setup used to characterize the stretchable photonic devices. The two ends of the fabricated devices in the form of stretchable membranes were mounted to a couple of linear motion stages. Nominal tensile strain applied on the membrane was controlled by changing the distance between the two motion stages. A pair of single-mode fiber probes with cleaved end facets were used to couple light from an external cavity tunable laser (Luna Technologies) to the devices via grating couplers and back to an optical vector analyzer for spectrally resolved transmittance measurement. Figure 1f shows a stretched device under test.

Finite element modeling

To obtain the strain field of the stretchable photonics, we have conducted numerical simulations with finite element method (FEM) using the commercial software ABAQUS v6.14. The elastic properties of materials used in the simulations are either quoted from the manufacturer's specifications (for SU-8) or experimentally measured using dynamic mechanical analysis (for PDMS) or the ultrasound pulse-echo technique (for $Ge_{23}Sb_7S_{70}$). The stretchable photonic devices embedded in a PDMS matrix were modeled. Taking geometric symmetry into account, only half of the device and the matrix were needed in the simulation, which reduces the computational cost. Moreover, since SU-8 and $Ge_{23}Sb_7S_{70}$ glass have similar mechanical properties, the photonic device was modeled as a device made of SU-8 only. As discussed in Results and Discussion section, SU-8 is much stiffer than the PDMS matrix, therefore, upon a far-field load, strains in the PDMS matrix are expected to be much larger compared to that of the photonic device. Thus, the device material (SU-8) was considered linear elastic whereas PDMS was modeled as incompressible Neo-Hookean material. C3D4 and C3D4H elements were used to mesh the photonic device and the PDMS matrix, respectively. To elucidate the superior mechanical robustness of the device, a 41% uniaxial tensile strain, which is far beyond the failure strain of the device materials, was applied to the matrix in the far field. At equilibrium status, strains in the device was computed and shown in Figure 2.

RESULTS AND DISCUSSION

Design considerations and fabrication protocols

The fabrication flow of stretchable photonic devices is schematically illustrated in Figure 3, and details of the process are furnished in Materials and Methods section. In the following we summarize the key fabrication steps and our rationale for material choices and device design.

The process starts with a handler silicon wafer on which a polydimethylsiloxane (PDMS) elastomer layer and an SU-8 epoxy film are sequentially coated. The PDMS layer acts as the stretchable substrate; and the SU-8 epoxy film fulfills several functions. First, it has an intermediate CTE of 52 ppm $°C^{-1}$, which lies between those of the $Ge_{23}Sb_7S_{70}$ chalcogenide glass (17.1 ppm $°C^{-1}$) and PDMS (310 ppm $°C^{-1}$)[39]. In effect, the epoxy film serves as a thermal stress release layer to bridge the large CTE mismatch between the glass and PDMS. The stress suppression effect is evident from our own

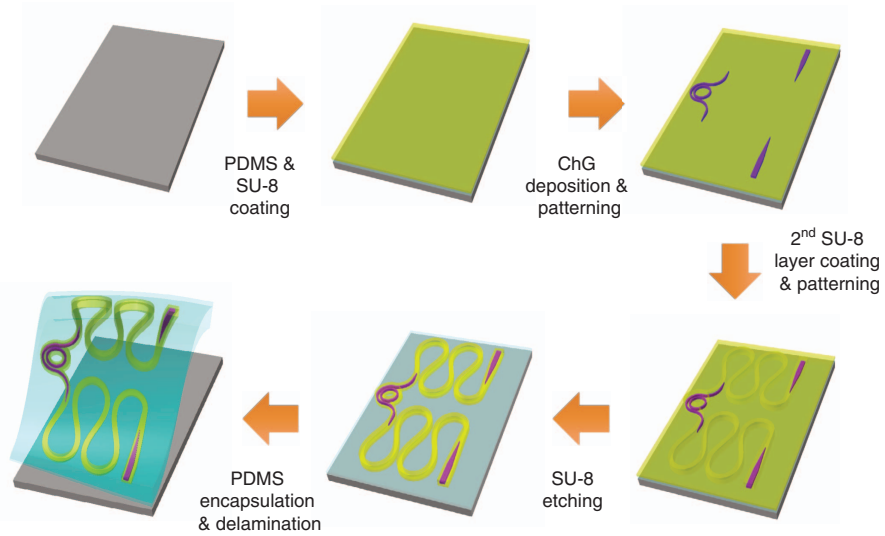

Figure 3 Schematic fabrication process flow of the stretchable photonic devices.

fabrication results: in the absence of the SU-8 layer, ChG films deposited and patterned directly on PDMS suffer from severe damage, whereas no cracks were visible under optical microscope inspection in structures containing the SU-8 buffer layer (Supplementary Information Section I). In addition, SU-8 is mechanically rugged with a Young's modulus of 2.0 GPa, close to that of $Ge_{23}Sb_7S_{70}$ glass (16.4 GPa) and much higher than that of PDMS (2.6 MPa). Therefore, lithographically patterned SU-8 pads provide the locally stiff 'islands' on which the critical optical components locate. Finally, SU-8 is optically transparent and has a refractive index of 1.57 (measured at 1310 and 1550 nm telecommunication bands), slightly higher than that of PDMS (1.40). SU-8 can thus function as a low-index-contrast waveguide core for light transmission.

We recognize that the combination of SU-8 and PDMS, while suitable for low loss waveguiding, does not offer sufficient index contrast for optical functions such as diffractive coupling, tight waveguide bends, or a complete photonic bandgap. A $Ge_{23}Sb_7S_{70}$ chalcogenide glass film with a refractive index of 2.22 (measured at 1550 nm wavelength) is subsequently deposited and lithographically patterned to form HIC structures (for example, grating couplers). In these HIC components, the SU-8 epoxy is used simultaneously as the optical cladding and as mechanical support to locally stiffen the substrate and minimize undesired geometric deformations as well as ensuing strain-induced operation wavelength drift. We further note that while here we chose the specific glass composition of $Ge_{23}Sb_7S_{70}$, monolithic integration of ChG photonics on epoxy films had been previously validated in several ChG composition groups[16], thereby offering significant flexibility for optical design and device engineering. To facilitate optical coupling between the low-index-contrast SU-8/PDMS waveguides and HIC ChG/SU-8 elements, we designed and fabricated adiabatic mode transformers with a low insertion loss of (0.4 ± 0.2) dB per coupler (Supplementary Information Section II).

In the next step, a second SU-8 epoxy layer is spin-coated and patterned to serve both as the top optical cladding for the ChG devices and as an etch mask to define serpentine waveguide structures in the bottom SU-8 layer. Here the advantage of using SU-8 as the etch mask is that itself is also an electron beam resist and thus can be readily patterned via electron beam writing. The serpentine waveguide layout is designed to enhance mechanical stretchability of the structure. In stretchable electronics, a horseshoe design consisting of piecewise circular segments have been optimized for maximizing stretchability of metal wires[40]. When applied to optical waveguides, the design nevertheless results in excessive radiative optical loss due to the abrupt curvature change at the junctions between the circular arcs. To mitigate such scattering losses, waveguide structures with continuously varying curvature following Bezier curve or Euler spiral geometries have been adopted[41,42]. We therefore implemented an Euler spiral design in our serpentine waveguide layout, which allows up to 64% propagation loss reduction compared with the traditional horseshoe structures while contributing to large stretchability (Supplementary Information Section III).

Finally, the fabricated devices are encapsulated by a second PDMS layer and delaminated from the handler wafer in the form of freestanding stretchable membranes for optical and mechanical characterizations.

Optical and mechanical characterizations

Figure 1a and 1b shows optical micrographs of a sample in its undeformed state. As shown in the figure, a typical device under test comprises a micro-ring resonator connected to two grating couplers through meandering waveguides assuming an Euler spiral geometry. The grating couplers and the micro-ring resonator are encapsulated in SU-8 islands to minimize shape distortion during stretching. The grating couplers are optimized for TE polarized light and fabricated using $Ge_{23}Sb_7S_{70}$ glass embedded in SU-8, whereas two types of

doi:10.1038/lsa.2017.138

micro-ring resonators made of SU-8/PDMS (core/cladding) and ChG/SU-8, respectively, are fabricated and tested.

During optical testing, TE-polarized laser light was coupled into the stretchable devices via ChG grating couplers embedded in the SU-8 layer. The sample was mounted on a pair of linear translational stages which precisely controlled the nominal mechanical strain (defined as the fractional elongation of the entire sample along the stretching direction) applied on the sample (Figure 1e and Materials and Methods section). Figure 1g compares the measured intrinsic quality factors (Q's) of the SU-8/PDMS and ChG/SU-8 resonators at 1310 and 1550 nm wavelengths. Our results obtained in the SU-8/PDMS devices are comparable to the best previously reported Q values in SU-8 resonators on rigid substrates[43–46]. The lower Q-factor of SU-8/PDMS rings at 1550 nm is attributed to C-H bond overtone absorption in SU-8[43].

For comparison, optical performance of the devices was also monitored as the samples underwent tensile strain. Figure 1c and 1d shows optical microscope images of a device at 36% nominal strain. While shape change of the serpentine waveguides is apparent, no cracks or defects were visually discernable during or after repeated stretching (Supplementary Information Section IV). Figure 1h presents the transmission spectra of a ChG/SU-8 resonator under different strains. The waveguide propagation loss remained unchanged at different strain states. We note that the resonant peak red shifts with increasing strain: such strain-optical coupling behavior is quantitatively accounted for using a model detailed in a succeeding section. Figure 1i plots the measured intrinsic Q-factors of the resonator. No measurable change was observed after 3000 stretching cycles at 41% nominal strain, which attests to the exceptional mechanical ruggedness of the device.

Mechanical modeling

We constructed finite element method (FEM) models to elucidate the superior mechanical robustness of the device despite the intrinsic brittleness of its constituent materials. Details of the FEM modeling is described in Materials and Methods section. Figure 2a depicts the strain distribution in a half-period Euler spiral structure. With 41% overall structure elongation, the maximum strain in the Euler spiral structure is only 3%: this 14-fold strain reduction clearly signifies the strain suppression efficacy of the design. To evaluate the effect of local substrate stiffening, we also modeled the stretching behavior of the device layout shown in Figure 1a. Figure 2b maps the strain fields in the SU-8 'islands' and Figure 2d plots the local stresses along the ChG micro-ring embedded inside the SU-8 supporting structure, both calculated at 41% elongation of the entire device. The stresses along the micro-ring correspond to an average strain of merely 0.77%, 55 times lower than the nominal strain exerted on the structure. We therefore conclude that local substrate stiffening is highly effective in stabilizing the operation of photonic devices whose optical characteristics are sensitive to geometric deformation.

Strain-optical coupling in flexible photonic devices: a predictive model

As shown in Figure 1h, the resonant peak of the micro-ring device red shifts with increasing tensile strain. Similar strain-optical coupling response has also been reported and theoretically analyzed in several prior publications[13,16,47–49]. According to the theoretical models[13,48], there are three effects contributing to the observed strain-optical coupling: strain-induced waveguide effective index and length changes due to dimensional variations, and photoelastic effect which modifies the refractive indices of waveguide core and cladding materials. While the physics of such coupling is relatively well-established, these models suffer from a major drawback: they are unable to provide quantitative predictions on the strain-optical coupling characteristics and can only be used to fit experimentally measured data retrospectively. The key challenge resides in accurate assessment of photoelastic effects in thin film materials: the sub-micron thickness of optical thin films renders traditional phase retardation analysis techniques[50] unreliable for quantifying the weak photoelastic interactions in most inorganic materials (for example, the stress-optical coefficient is in the order of 10^{-12} Pa^{-1} in inorganic glasses, one to two orders of magnitude smaller than the typical values in polymers). A technique involving temperature-dependent prism coupling measurements performed on the same film deposited on multiple different substrate materials was devised[51], although it has poor accuracy (due to the limited refractive index resolution of prism coupling at $>10^{-4}$) and mandates prior knowledge about the film and substrates (including elastic moduli, Poisson ratio, CTE and so on) which may not be readily available. In addition to the difficulties associated with extracting photoelastic parameters, these early models also only consider the oversimplified case of uniform strain and neglect the tensorial nature of strain and stress.

Here we developed a tensorial stress-optical coupling model generically applicable to arbitrary spatially varying stress profiles and waveguide geometries. The theoretical derivation is presented in Supplementary Information Section V. For the sake of brevity, we directly quote the general result of resonance wavelength shift caused by applied stress σ:

$$\mathrm{d}\lambda_0 = \sum_i \frac{\lambda_0}{L_{\mathrm{tot}} n_{\mathrm{g}}} \int_L \left(n_{\mathrm{eff}} \frac{\partial \varepsilon_L}{\partial \sigma_i} + \frac{\partial n_{\mathrm{eff}}}{\partial \sigma_i} \right) \sigma_i(L) \mathrm{d}L \tag{1}$$

where λ_0 represents the resonant wavelength (in free space), L_{tot} is the resonator length, n_{g} and n_{eff} are the modal group and effective indices respectively, ε_L denotes axial strain along the waveguide, and the contour integral is carried out along the resonator waveguide path. In Equation (1), the summation is performed over all normal stress tensor components, as we have proven that shear stress components have a negligible impact on waveguiding properties of photonic devices (Supplementary Information Section VI). Here we formulate the problem in terms of stress instead of strain because normal stress in the surface-normal direction vanishes in flexible photonic systems taking the form of a freestanding membrane, which is evidenced by the FEM results in Figure 2d showing that σ_z is negligible compared with σ_R or σ_θ. Therefore, for a circularly symmetric micro-ring resonator the summation in Equation (1) reduces to:

$$\mathrm{d}\lambda_0 = \frac{\lambda_0}{L_{\mathrm{tot}} n_{\mathrm{g}}} \int_0^{2\pi} [C_R \sigma_R(L) + C_\theta \sigma_\theta(L)] R \mathrm{d}\theta \tag{2}$$

where R is the resonator radius in the absence of perturbation and the two stress-optical coupling coefficients C are defined as:

$$C_R = n_{\mathrm{eff}} \frac{\partial \varepsilon_L}{\partial \sigma_R} + \frac{\partial n_{\mathrm{eff}}}{\partial \sigma_R} \tag{3}$$

and

$$C_\theta = n_{\mathrm{eff}} \frac{\partial \varepsilon_L}{\partial \sigma_\theta} + \frac{\partial n_{\mathrm{eff}}}{\partial \sigma_\theta} \tag{4}$$

which represent the stress-optical coupling strength in the radial (R) and circumferential (θ) directions of the resonator (Figure 2c), respectively.

To quantify the two stress-optical coupling coefficients, we employed a calibration sample encompassing two sets of Fabry-Perot (F-P) waveguide Bragg cavities oriented in orthogonal

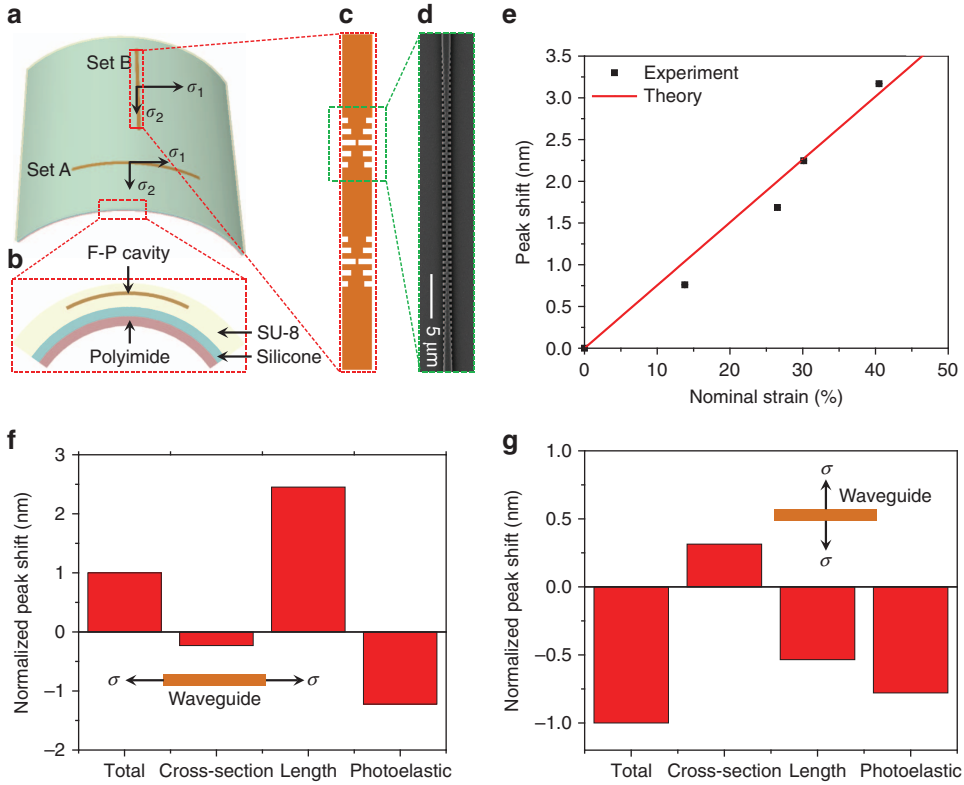

Figure 4 (**a**) Schematic layout of the calibration sample; (**b**) cross-sectional structure of the calibration sample; (**c**) schematic illustration of the F-P cavity design, which consists of a straight waveguide segment situated between a pair of Bragg grating reflectors; (**d**) top-view SEM micrograph of the waveguide Bragg grating reflector; (**e**) comparison of the experimentally determined strain-induced resonance shifts according to Figure 1h (points) and our theoretical prediction (solid line). Note that the theory does not involve any fitting parameters from the stretchable device measurement; (**f**, **g**) calculated relative contributions of photoleastic effects, waveguide cross-sectional modification, and waveguide length change to overall strain-induced resonance shift (normalized as unity) when in-plane uniaxial tensile stress is applied **f** along the resonator waveguide and **g** perpendicular to the waveguide. The positive/negative signs indicate red/blue shifts, respectively. Insets illustrate the stressed waveguide configurations.

directions, as illustrated in Figure 4a. Each set consists of F-P cavities of varying lengths to eliminate stress-optical coupling contributions from the Bragg reflectors, and the waveguide sections in the cavities have a uniform cross-sectional geometry identical to that of the micro-ring resonator. The sample was bent to a series of radii and the corresponding resonance drifts of the two sets of cavities were monitored. As discussed in Supplementary Information Section VII, such stress-induced resonance shifts in the two orthogonal sets of devices allow us to independently evaluate the two stress-optical coupling constants C_R and C_θ. The measured C_R and C_θ values and spatially varying stress field along the micro-ring simulated using FEM (Figure 2d) were then substituted into Equation (2) to predict the resonance wavelength shift in stretchable devices shown in Figure 1h. Figure 4e compares the theoretical predictions made using Equation (2) (solid line) and the measured resonance shift from Figure 1h (dots), and the excellent agreement substantiates our stress-optical coupling theory. We note that the theoretical prediction in Figure 4e was made solely based on either experimentally measured parameters on the calibration sample or FEM simulation results rather than data from the stretchable device under investigation, and therefore our model can indeed be applied to predict strain-optical coupling behavior in flexible photonic devices.

Our approach also offers an accurate route to quantify photoelastic effects in the waveguide materials (refer to Supplementary Information Section VIII for detailed analysis procedures). Figure 4f and 4g delineates the relative contributions of photoleastic effects, waveguide cross-sectional geometry modification, and waveguide length change to overall resonance shift (normalized as unity) when in-plane uniaxial tensile stress is applied along the resonator waveguide (Figure 4f) and perpendicular to the waveguide (Figure 4g). Notably, in the latter case tensile stress produces blue detuning of the cavity resonance because of Poisson's effect and refractive index decrease due to photoelasticity. Error analysis based on our experimental data reveals that our technique can measure stress-optical coefficients with an accuracy down to 10^{-12} Pa^{-1} (Supplementary Information Section IX), qualifying it as a highly sensitive method for characterizing photoelasticity in thin film optical devices.

CONCLUSIONS

In conclusion, we have demonstrated the first single-mode stretchable integrated photonic devices. The stretchable photonics platform has been implemented in two material systems: high-index chalcogenide glasses and low-index epoxy polymers, both monolithically integrated on PDMS elastomer substrates. We have further realized low-loss optical coupling and seamless co-integration of the two systems on a common substrate platform. Our unique approach allows significant design flexibility to garner performance gains from both high-index-contrast and low-index-contrast photonic designs.

doi:10.1038/lsa.2017.138

Our micro-mechanical engineering strategies towards enhancing stretching capabilities involve local substrate stiffening to protect functional photonic components, and an Euler spiral based interconnecting waveguide design which effectively suppresses both local strain and radiative optical loss. Photonic devices fabricated following this configuration exhibit remarkable mechanical ruggedness and can readily withstand 3000 stretching cycles at 41% nominal strain without compromising their structural integrity and optical performance. Our design approach is also non-material-specific and can be generically applied to transform intrinsically rigid or brittle materials into a highly stretchable and optically functional form.

Finally, we have also derived and experimentally verified a rigorous theory enabling predictive modeling of strain-optical coupling behavior in photonic devices for the first time. The theory is widely applicable to soft materials and mechanically compliant device architectures in photonics, which are becoming increasingly prevalent as integrated photonics continues to penetrate emerging applications such as biomedicine, sensing, and short-reach communications.

CONFLICT OF INTEREST

The authors declare no conflict of interest.

AUTHOR CONTRIBUTIONS

LL and HL conceived the device designs and carried out device fabrication and testing. SQ performed mechanical modeling and analysis. YH, CR and LV assisted in device testing. JL and JM contributed to thin film deposition. AY synthesized and characterized the glass materials. JH, TG, NL and KR supervised and coordinated the project. All authors contributed to writing the paper.

ACKNOWLEDGEMENTS

The authors gratefully thank Lionel C Kimerling and Anu Agarwal for providing access to device measurement facilities, Qingyang Du and Derek Kita for assistance with device processing and characterization, and Mark Mondol for technical support with electron beam lithography. Funding support is provided by the National Science Foundation under award numbers 1453218, 1506605, and 1351875. The authors also acknowledge fabrication facility support by the MIT Microsystems Technology Laboratories and the Harvard University Center for Nanoscale Systems, the latter of which is supported by the National Science Foundation under award 0335765.

1 Hu JJ, Li L, Lin HT, Zhang P, Zhou WD *et al.* Flexible integrated photonics: where materials, mechanics and optics meet [Invited]. *Opt Mater Express* 2013; **3**: 1313–1331.
2 Li L, Lin HT, Michon J, Huang YZ, Li JY *et al.* A new twist on glass: a brittle material enabling flexible integrated photonics. *Int J Appl Glass Sci* 2017; **8**: 61–68.
3 Dangel R, Horst F, Jubin D, Meier N, Weiss J *et al.* Development of versatile polymer waveguide flex technology for use in optical interconnects. *J Lightwave Technol* 2013; **31**: 3915–3926.
4 Swatowski BW, Amb CM, Breed SK, Deshazer DJ, Weidner WK *et al.* Flexible, stable, and easily processable optical silicones for low loss polymer waveguides. *Proc SPIE* 2013; **8622**: 862205.
5 Li L, Zou Y, Lin HT, Hu JJ, Sun XC *et al.* A fully-integrated flexible photonic platform for chip-to-chip optical interconnects. *J Lightwave Technol* 2013; **31**: 4080–4086.
6 Choi C, Lin L, Liu YJ, Choi J, Wang L *et al.* Flexible optical waveguide film fabrications and optoelectronic devices integration for fully embedded board-level optical interconnects. *J Lightwave Technol* 2004; **22**: 2168–2176.
7 Shibata T, Takahashi A. Flexible opto-electronic circuit board for in-device interconnection. *58th Electronic Components and Technology Conference*, 27-30 May 2008; Lake Buena Vista, FL, USA. IEEE: New York, NY, USA, 2008, pp261–pp267.
8 Bosman E, van Steenberge G, van Hoe B, Missinne J, Vanfleteren J *et al.* Highly reliable flexible active optical links. *IEEE Photonics Technol Lett* 2010; **22**: 287–289.
9 Chen Y, Li H, Li M. Flexible and tunable silicon photonic circuits on plastic substrates. *Sci Rep* 2012; **2**: 622.
10 Zhu L, Kapraun J, Ferrara J, Chang-Hasnain CJ. Flexible photonic metastructures for tunable coloration. *Optica* 2015; **2**: 255–258.
11 Zou Y, Moreel L, Lin HT, Zhou J, Li L *et al.* Solution processing and resist-free nanoimprint fabrication of thin film chalcogenide glass devices: inorganic-organic hybrid photonic integration. *Adv Opt Mater* 2014; **2**: 759–764.
12 Gao L, Zhang YH, Malyarchuk V, Jia L, Jang KI *et al.* Epidermal photonic devices for quantitative imaging of temperature and thermal transport characteristics of the skin. *Nat Commun* 2014; **5**: 4938.
13 Fan L, Varghese LT, Xuan Y, Wang J, Niu B *et al.* Direct fabrication of silicon photonic devices on a flexible platform and its application for strain sensing. *Opt Express* 2012; **20**: 20564–20575.
14 Kamali SM, Arbabi A, Arbabi E, Horie Y, Faraon A. Decoupling optical function and geometrical form using conformal flexible dielectric metasurfaces. *Nat Commun* 2016; **7**: 11618.
15 Zhou WD, Ma ZQ. Breakthroughs in photonics 2012: breakthroughs in nanomembranes and nanomembrane lasers. *IEEE Photonics J* 2013; **5**: 0700707.
16 Li L, Lin HT, Qiao ST, Zou Y, Danto S *et al.* Integrated flexible chalcogenide glass photonic devices. *Nat Photonics* 2014; **8**: 643–649.
17 Zou Y, Zhang DN, Lin HT, Liu L, Moreel L *et al.* High-performance, high-index-contrast chalcogenide glass photonics on silicon and unconventional non-planar substrates. *Adv Opt Mater* 2014; **2**: 478–486.
18 Li L, Zhang P, Wang WM, Lin HT, Zerdoum AB *et al.* Foldable and cytocompatible sol-gel TiO_2 photonics. *Sci Rep* 2015; **5**: 13832.
19 Arumugam V, Naresh MD, Sanjeevi R. Effect of strain rate on the fracture behaviour of skin. *J Biosci* 1994; **19**: 307–313.
20 Missinne J, Kalathimekkad S, van Hoe B, Bosman E, Vanfleteren J *et al.* Stretchable optical waveguides. *Opt Express* 2014; **22**: 4168–4179.
21 Zhao HC, O'Brien K, Li S, Shepherd RF. Optoelectronically innervated soft prosthetic hand via stretchable optical waveguides. *Sci Rob* 2016; **1**: eaai7529.
22 Yu CL, Kim H, de Leon N, Frank IW, Robinson JT *et al.* Stretchable photonic crystal cavity with wide frequency tunability. *Nano Lett* 2013; **13**: 248–252.
23 Gutruf P, Zou CJ, Withayachumnankul W, Bhaskaran M, Sriram S *et al.* Mechanically tunable dielectric resonator metasurfaces at visible frequencies. *ACS Nano* 2016; **10**: 133–141.
24 Ee HS, Agarwal R. Tunable metasurface and flat optical zoom lens on a stretchable substrate. *Nano Lett* 2016; **16**: 2818–2823.
25 Chen WQ, Lam RH, Fu JP. Photolithographic surface micromachining of polydimethylsiloxane (PDMS). *Lab Chip* 2012; **12**: 391–395.
26 Chou N, Kim Y, Kim S. A method to pattern silver nanowires directly on wafer-scale PDMS substrate and its applications. *ACS Appl Mater Interfaces* 2016; **8**: 6269–6276.
27 Tinku S, Collini C, Lorenzelli L, Dahiya RS. Smart contact lens using passive structures. *2014 IEEE SENSORS*, 2-5 November 2014; Valencia, Spain Valencia, Spain. IEEE: New York, NY, USA, 2014, pp2107–pp2110.
28 Jung SW, Koo JB, Park CW, Na BS, Oh JY *et al.* Flexible organic thin-film transistors fabricated on polydimethylsiloxane elastomer substrates. *J Nanosci Nanotechnol* 2015; **15**: 7513–7517.
29 Romeo A, Liu QH, Suo ZG, Lacour SP. Elastomeric substrates with embedded stiff platforms for stretchable electronics. *Appl Phys Lett* 2013; **102**: 131904.
30 Gray DS, Tien J, Chen CS. High-conductivity elastomeric electronics. *Adv Mater* 2004; **16**: 393–397.
31 Kim DH, Lu NS, Ghaffari R, Kim YS, Lee SP *et al.* Materials for multifunctional balloon catheters with capabilities in cardiac electrophysiological mapping and ablation therapy. *Nat Mater* 2011; **10**: 316–323.
32 Verplancke R, Bossuyt F, Cuypers D, Vanfleteren J. Thin-film stretchable electronics technology based on meandering interconnections: fabrication and mechanical performance. *J Micromech Microeng* 2011; **22**: 015002.
33 Kim DH, Ghaffari R, Lu NS, Rogers JA. Flexible and stretchable electronics for biointegrated devices. *Annu Rev Biomed Eng* 2012; **14**: 113–128.
34 Huang M. Stress effects on the performance of optical waveguides. *Int J Solids Struct* 2003; **40**: 1615–1632.
35 Ye WN, Xu DX, Janz S, Cheben P, Picard MJ *et al.* Birefringence control using stress engineering in silicon-on-insulator (SOI) waveguides. *J Lightwave Technol* 2005; **23**: 1308–1318.
36 Hu JJ, Tarasov V, Agarwal A, Kimerling L, Carlie N *et al.* Fabrication and testing of planar chalcogenide waveguide integrated microfluidic sensor. *Opt Express* 2007; **15**: 2307–2314.
37 Musgraves J, Carlie N, Hu J, Petit L, Agarwal A *et al.* Comparison of the optical, thermal and structural properties of Ge-Sb-S thin films deposited using thermal evaporation and pulsed laser deposition techniques. *Acta Mater* 2011; **59**: 5032–5039.
38 Du QY, Huang YZ, Li JY, Kita D, Michon J *et al.* Low-loss photonic device in Ge-Sb-S chalcogenide glass. *Opt Lett* 2016; **41**: 3090–3093.
39 Carlie NA. *A Solution-based Approach to the Fabrication of Novel Chalcogenide Glass Materials and Structures*. PhD dissertation, Clemson University, Clemson, USA, 2010.
40 Gonzalez M, Axisa F, Bulcke MV, Brosteaux D, Vandevelde B *et al.* Design of metal interconnects for stretchable electronic circuits. *Microelectron Reliab* 2008; **48**: 825–832.
41 Klein S, Barsella A, Leblond H, Bulou H, Fort A *et al.* One-step waveguide and optical circuit writing in photopolymerizable materials processed by two-photon absorption. *Appl Phys Lett* 2005; **86**: 211118.
42 Cherchi M, Ylinen S, Harjanne M, Kapulainen M, Aalto T. Dramatic size reduction of waveguide bends on a micron-scale silicon photonic platform. *Opt Express* 2013; **21**: 17814–17823.
43 Rabiei P, Steier WH, Zhang C, Dalton LR. Polymer micro-ring filters and modulators. *J Lightwave Technol* 2002; **20**: 1968–1975.
44 Girault P, Lorrain N, Poffo L, Guendouz M, Lemaitre J *et al.* Integrated polymer micro-ring resonators for optical sensing applications. *J Appl Phys* 2015; **117**: 104504.

45 Poon JKS, Huang YY, Paloczi GT, Yariv A. Soft lithography replica molding of critically coupled polymer microring resonators. *IEEE Photonics Technol Lett* 2004; **16**: 2496–2498.
46 Jin L, Fu X, Yang B, Shi YC, Dai DX. Optical bistability in a high-*Q* racetrack resonator based on small SU-8 ridge waveguides. *Opt Lett* 2013; **38**: 2134–2136.
47 De Brabander GN, Boyd JT, Beheim G. Integrated optical ring resonator with micromechanical diaphragms for pressure sensing. *IEEE Photonics Technol Lett* 1994; **6**: 671–673.
48 Westerveld WJ, Leinders SM, Muilwijk PM, Pozo J, van den Dool TC *et al*. Characterization of integrated optical strain sensors based on silicon waveguides. *IEEE J Sel Top Quant Electron* 2014; **20**: 5900110.
49 Bhola B, Song HC, Tazawa H, Steier WH. Polymer microresonator strain sensors. *IEEE Photonics Technol Lett* 2005; **17**: 867–869.
50 Tsukiji M, Kowa H, Muraki K, Umeda N, Imoto K *et al*. Measurement system for very small photoelastic constant of polymer films. *Macromol Symp* 2006; **242**: 235–240.
51 Hossain MF, Chan HP, Uddin MA. Simultaneous measurement of thermo-optic and stress-optic coefficients of polymer thin films using prism coupler technique. *Appl Opt* 2010; **49**: 403–408.

Supplementary Information for this article can be found on the *Light: Science & Applications*' website (http://www.nature.com/lsa).

Supplementary Information for

Monolithically Integrated Stretchable Photonics

Lan Li[1†,*], Hongtao Lin[1†], Shutao Qiao[2†], Yi-Zhong Huang[1,3], Jun-Ying Li[1,4], Jérôme Michon[1], Tian Gu[1], Carlos Alosno-Ramos[5], Laurent Vivien[5], Anupama Yadav[6], Kathleen Richardson[6], Nanshu Lu[2], Juejun Hu[1,*]

[1]Department of Materials Science & Engineering, Massachusetts Institute of Technology, Cambridge, Massachusetts, USA
[2]Department of Aerospace Engineering and Engineering Mechanics, University of Texas at Austin, Austin, Texas, USA
[3]Department of Electronic Engineering, Xiamen University, Xiamen, China
[4]Key Laboratory of Optoelectronic Technology & System, Education Ministry of China, Chongqing University, Chongqing, China
[5]Centre for Nanoscience and Nanotechnology, CNRS, Univ. Paris-Sud, Universite Paris-Saclay, C2N – Orsay, Orsay cedex, France
[6]The College of Optics & Photonics, University of Central Florida, Orlando, Florida, USA

† These authors contributed equally to this work.
**lanli1@mit.edu, hujuejun@mit.edu*

In this Supplementary Information, we provide further details on device modeling, fabrication, and characterization results. This Supplementary Information comprises the following Sections:

I. Direct photonic device fabrication on PDMS: the impact of SU-8 buffer layer

II. Adiabatic coupling between low-index-contrast and high-index-contrast optics

III. Optical loss comparison in circular and Euler spiral waveguide bends

IV. Structural integrity of devices after 3,000 stretching cycles

V. Derivation of strain-optical coupling theory in guided wave photonic devices

VI. Coupling of shear stresses to optical modes

VII. Extracting C_R and C_θ from calibration sample measurements

VIII. Quantification of strain-optical coupling contributions from geometric and photoelastic terms

IX. Error analysis of stress-optical coefficient measurement

Section I – Direct photonic device fabrication on PDMS: the impact of SU-8 buffer layer

Direct deposition and lithographic patterning of $Ge_{23}Sb_7S_{70}$ chalcogenide glass were attempted on PDMS films coated on a silicon handler wafer. While we were able to obtain crack-free $Ge_{23}Sb_7S_{70}$ films on PDMS via thermal evaporation (as the substrates were held near room temperature during deposition), subsequent lithographic processing resulted in extensive cracking throughout the samples (Figs. S1a-S1c). This is presumably caused by the large CTE mismatch between $Ge_{23}Sb_7S_{70}$ glass (17.1 ppm $°C^{-1}$) and PDMS (310 ppm $°C^{-1}$), which leads to thermal stress accumulation during resist baking steps.

The cracking issue is resolved by inserting a cured SU-8 layer between the $Ge_{23}Sb_7S_{70}$ film and the PDMS substrate. Once cured, SU-8 becomes a robust thermosetting polymer with a tensile strength of 60 MPa[1]. Since the maximum thermal stress in the film is estimated to be less than 0.4 MPa based on our processing temperature, the SU-8 layer can maintain its structural integrity and inhibit crack initiation. SU-8 also has an intermediate CTE of 52 ppm $°C^{-1}$, and the reduced CTE mismatch between SU-8 and $Ge_{23}Sb_7S_{70}$ glass effectively prevent damage of the glass film. As shown in Fig. S1d, $Ge_{23}Sb_7S_{70}$ glass structured defined on SU-8/PDMS exhibit excellent pattern fidelity with no sign of cracking.

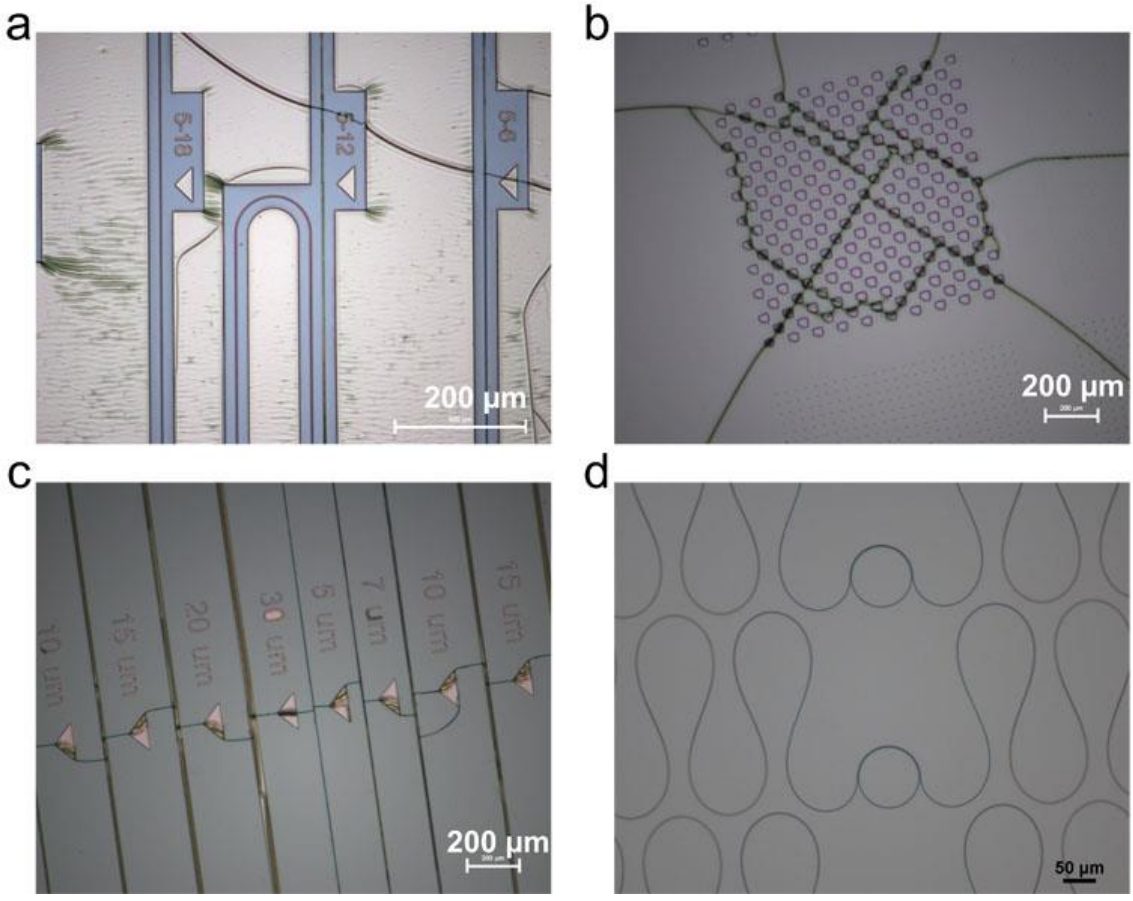

Figure S1. (a-c) Micrographs of $Ge_{23}Sb_7S_{70}$ glass patterns directly fabricated on PDMS; (d) $Ge_{23}Sb_7S_{70}$ glass waveguides fabricated on SU-8 as a buffer layer on top of PDMS.

Section II – Adiabatic coupling between low-index-contrast and high-index-contrast optics

Low-loss transition between the high-index-contrast ChG/SU-8 waveguides and the low-index-contrast SU-8/PDMS guides is realized via an adiabatic mode transformer. The mode size converter made of $Ge_{23}Sb_7S_{70}$ glass embedded in an SU-8 strip waveguide and assumes an inverse taper geometry. The ChG/SU-8 waveguide and mode transformer design parameters are illustrated in Fig. S2. The same set of geometric parameters were adopted for stretchable devices described throughout this article.

Insertion loss of the mode transformer is measured by taking the difference of optical transmittances (in dB) through the structures depicted in Fig. S2b and Fig. S2a of the same total length. Five pairs of devices with identical configurations were measured, yielding an average insertion loss of (0.4 ± 0.2) dB for the mode transformer.

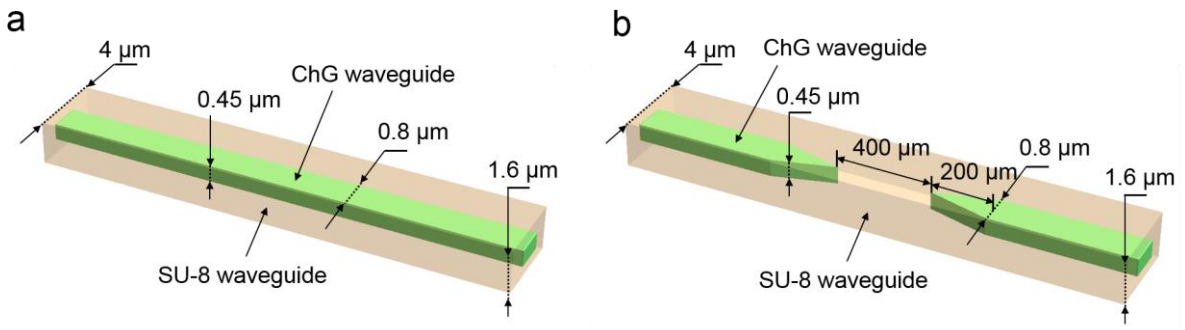

Figure S2. Waveguide and mode transformer design: (a) a ChG/SU-8 waveguide; and (b) two mode transformers connected back-to-back in series for insertion loss characterization.

Section III – Optical loss comparison in circular and Euler spiral waveguide bends

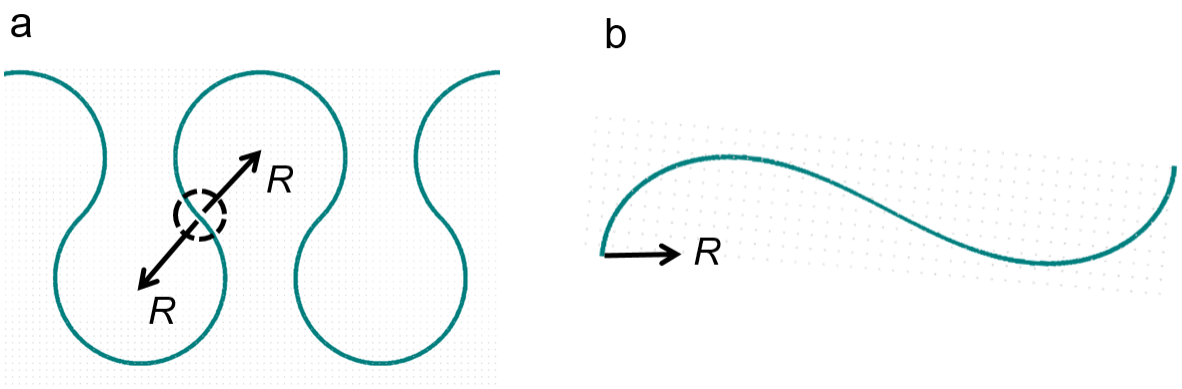

Figure S3. Two meandering ChG/SU-8 waveguide configurations for stretchable photonics comprising (a) circular segments; and (b) Euler spirals (the graph shows half a period).

Figures S3a and S3b illustrate the two meandering ChG/SU-8 waveguide configurations under comparison, where *R* denotes the local radius curvature. Propagation losses in the waveguides were measured using a "cut-back" method in serpentine waveguides containing varying numbers of bending segments (repeating units). Table S1 summarizes measured losses in the devices. The much higher propagation loss in the serpentine waveguides consisting of circular segments is attributed to mode mismatch at the abrupt junctions between the circular segments. At 50 μm bending radius, the Euler spiral design has a loss figure similar to that of straight $Ge_{23}Sb_7S_{70}$ glass waveguides (~ 4 dB cm^{-1}). We have therefore adopted the Euler spiral structure with 50 μm bending radius to construct our stretchable photonic circuits.

Table S1. Measured optical propagation losses in serpentine ChG/SU-8 waveguides composed of circular and Euler spiral segments

	Radius *R* (μm)	Loss (dB cm^{-1})
Circular	25	12.5
Circular	50	7.7
Euler spiral	25	4.5
Euler spiral	50	4.3

Section IV – Structural integrity of devices after 3,000 stretching cycles

Figure S4 presents exemplary optical micrographs of serpentine waveguide structures after 3,000 stretching cycles at 41% nominal strain. Careful visual inspection through optical microscopy did not reveal any sign of cracking or delamination at different locations of the devices. No change in optical transmittance of the waveguides were detected after the repeated stretching cycles within our measurement error. These results attest to the superior mechanical ruggedness of our stretchable optical devices.

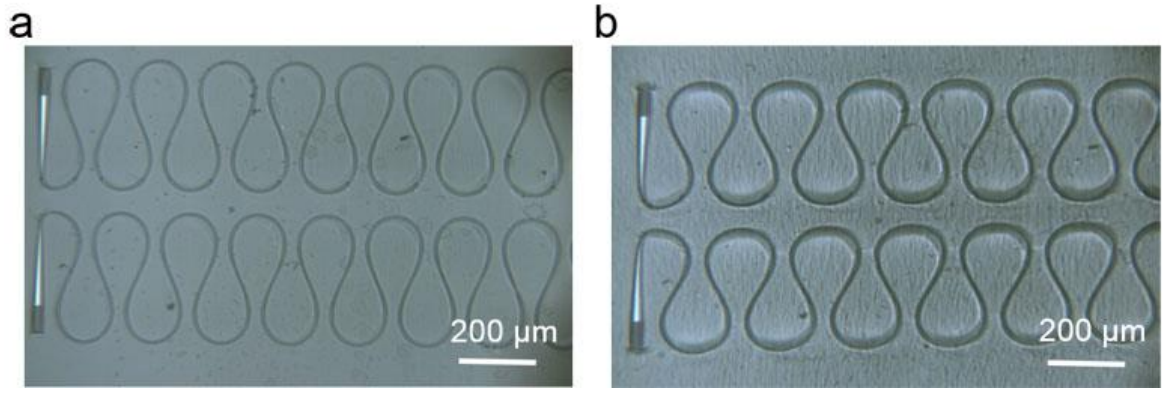

Figure S4. Optical microscope images of serpentine waveguides after 3,000 stretching cycles at 41% nominal strain (a) in its undeformed state; and (b) at 36% nominal strain. No cracks were visually observed in both cases.

Section V – Derivation of strain-optical coupling theory in guided wave photonic devices

In this section, we seek to derive a generic strain-optical coupling formalism which relates strain/stress fields to optical property changes of guided wave devices. For generality, here we consider spatially non-uniform strain/stress fields, take into account the tensorial nature of strains and stresses, and place no constraints on the geometric configurations of the waveguide structure. The following equations are derived for a travel-wave resonator, although the same analytical approach can be readily applied to other types of guided wave devices.

The resonant condition for a traveling wave resonator can be generically expressed as:

$$\int_{L_{\text{tot}}} n_{\text{eff}}\,\mathrm{d}L = N\lambda_0 \tag{1}$$

where the integral is performed along the length of the entire resonator. Here n_{eff} denotes the modal effective index, L_{tot} is the cavity length, λ_0 represents the resonant wavelength in free space, and N gives the longitudinal mode order. Linearity of the equation indicates that when a spatially varying perturbation to the optical path length is imposed on the resonator, the overall effect is equivalent to the sum of perturbative effects from each resonator segment dL. We therefore start with considering a stress-induced perturbation on one traveling wave resonator segment dL. The optical path length change caused by applied stress σ on the segment dL is:

$$\frac{\partial\left(n_{\text{eff}}\,\mathrm{d}L\right)}{\partial\sigma}\cdot\sigma = \left(n_{\text{eff}}\frac{\partial\varepsilon_L}{\partial\sigma} + \frac{\partial n_{\text{eff}}}{\partial\sigma} + \frac{\partial n_{\text{eff}}}{\partial\lambda_0}\frac{\partial\lambda_0}{\partial\sigma}\right)\cdot\sigma\,\mathrm{d}L \tag{2}$$

The three terms in the parentheses on the right-hand-side correspond to waveguide length change, stress-induced effective index modification (which include both photoelastic material index change and waveguide cross-sectional geometry deformation), and dispersive effects, respectively. ε_L denotes normal strain along the waveguide segment. The resulting resonant wavelength detuning is given by:

$$\int_{L_{\text{tot}}-\mathrm{d}L}\left(n_{\text{eff}} + \frac{\partial n_{\text{eff}}}{\partial\lambda_0}\cdot\mathrm{d}\lambda_{0,\mathrm{d}L}\right)\mathrm{d}L + n_{\text{eff}}\,\mathrm{d}L + \frac{\partial\left(n_{\text{eff}}\,\mathrm{d}L\right)}{\partial\sigma}\cdot\sigma = N\left(\lambda_0 + \mathrm{d}\lambda_{0,\mathrm{d}L}\right) \tag{3}$$

The first term on the left-hand-side manifests the dispersive effect imposed on the unperturbed waveguide segments. The integration is carried out along the resonator skipping the dL segment. Eq. 3 simplifies to:

$$\frac{\partial\left(n_{\text{eff}}\,\mathrm{d}L\right)}{\partial\sigma}\cdot\sigma = \left(N - \int_{L_{\text{tot}}-\mathrm{d}L}\frac{\partial n_{\text{eff}}}{\partial\lambda_0}\mathrm{d}L\right)\cdot\mathrm{d}\lambda_{0,\mathrm{d}L} \tag{4}$$

$$\Rightarrow\left(N - \int_{L_{\text{tot}}-\mathrm{d}L}\frac{\partial n_{\text{eff}}}{\partial\lambda_0}\mathrm{d}L\right)\cdot\mathrm{d}\lambda_{0,\mathrm{d}L} = \left(n_{\text{eff}}\frac{\partial\varepsilon_L}{\partial\sigma} + \frac{\partial n_{\text{eff}}}{\partial\sigma} + \frac{\partial n_{\text{eff}}}{\partial\lambda_0}\frac{\partial\lambda_0}{\partial\sigma}\right)\cdot\sigma\,\mathrm{d}L \tag{5}$$

$$\Rightarrow\left(N - \int_{L_{\text{tot}}}\frac{\partial n_{\text{eff}}}{\partial\lambda_0}\mathrm{d}L + \frac{\partial n_{\text{eff}}}{\partial\lambda_0}\mathrm{d}L\right)\cdot\mathrm{d}\lambda_{0,\mathrm{d}L} = \left(n_{\text{eff}}\frac{\partial\varepsilon_L}{\partial\sigma} + \frac{\partial n_{\text{eff}}}{\partial\sigma} + \frac{\partial n_{\text{eff}}}{\partial\lambda_0}\frac{\partial\lambda_0}{\partial\sigma}\right)\cdot\sigma\,\mathrm{d}L \tag{6}$$

Assuming that the unperturbed travel wave resonator is made up of waveguides with a uniform cross-section, we have:

$$n_{\text{eff}}L_{\text{tot}} = N\lambda_0 \tag{7}$$

Combining Eqs. 6 and 7 yields:

$$\left(\frac{n_{\text{eff}}L_{\text{tot}}}{\lambda_0} - \frac{\partial n_{\text{eff}}}{\partial\lambda_0}L_{\text{tot}} + \frac{\partial n_{\text{eff}}}{\partial\lambda_0}\mathrm{d}L\right)\cdot\mathrm{d}\lambda_{0,\mathrm{d}L} = \left(n_{\text{eff}}\frac{\partial\varepsilon_L}{\partial\sigma} + \frac{\partial n_{\text{eff}}}{\partial\sigma} + \frac{\partial n_{\text{eff}}}{\partial\lambda_0}\frac{\partial\lambda_0}{\partial\sigma}\right)\cdot\sigma\,\mathrm{d}L \tag{8}$$

Since the stress-induced effects can be treated as a high-order perturbation, we also have:

$$\frac{\partial \lambda_0}{\partial \sigma} = \frac{\mathrm{d}\lambda_{0,\mathrm{d}L}}{\sigma} \tag{9}$$

Eqs. 8 and 9 lead to:

$$\frac{L_{\mathrm{tot}}}{\lambda_0}\left(n_{\mathrm{eff}} - \lambda_0 \frac{\partial n_{\mathrm{eff}}}{\partial \lambda_0}\right)\cdot \mathrm{d}\lambda_{0,\mathrm{d}L} = \left(n_{\mathrm{eff}} \frac{\partial \varepsilon_L}{\partial \sigma} + \frac{\partial n_{\mathrm{eff}}}{\partial \sigma}\right)\cdot \sigma \mathrm{d}L \tag{10}$$

By definition, the waveguide group index is:

$$n_{\mathrm{g}} = n_{\mathrm{eff}} - \lambda_0 \frac{\partial n_{\mathrm{eff}}}{\partial \lambda_0} \tag{11}$$

Eq. 10 thereby simplifies to:

$$\mathrm{d}\lambda_{0,\mathrm{d}L} = \frac{\lambda_0}{L_{\mathrm{tot}} n_{\mathrm{g}}}\left(n_{\mathrm{eff}} \frac{\partial \varepsilon_L}{\partial \sigma} + \frac{\partial n_{\mathrm{eff}}}{\partial \sigma}\right)\cdot \sigma \mathrm{d}L \tag{12}$$

We note that the wavelength shift scales linearly with both the magnitude of the perturbation (σ) and the segment length dL, consistent with the linear nature of the resonant condition Eq. 1. Consequently, the total resonant wavelength shift when a stress field $\sigma(L)$ is exerted on the traveling wave resonator can be obtained through a line integration along the resonator perimeter:

$$\mathrm{d}\lambda_0 = \int_L \mathrm{d}\lambda_{0,\mathrm{d}L} = \frac{\lambda_0}{L_{\mathrm{tot}} n_{\mathrm{g}}} \int_L \left(n_{\mathrm{eff}} \frac{\partial \varepsilon_L}{\partial \sigma} + \frac{\partial n_{\mathrm{eff}}}{\partial \sigma}\right)\cdot \sigma(L)\mathrm{d}L \tag{13}$$

Here the spatial variation of σ is accounted for through the dependence of σ on L (denoting the location along the resonator). In the general case where multiple stress components co-exist, the left-hand-side should be the summation of individual stress component effects.

As an example, let's consider photonic devices fabricated on a thin membrane (as is the case for most flexible photonic devices as well as our stretchable devices). The geometric configuration supports in-plane biaxial stresses. For convenience, we employ a polar coordinate whose origin is located at the center of the micro-ring resonator (Fig. 3c). The two in-plane stress components are labeled as σ_R (normal stress along the in-plane transverse direction to the waveguide) and σ_θ (normal stress along the longitudinal direction along the waveguide). For the stretchable micro-ring resonator, Eq. 13 becomes:

$$\mathrm{d}\lambda_0 = \frac{\lambda_0}{L_{\mathrm{tot}} n_{\mathrm{g}}} \int_0^{2\pi} \left[C_R \cdot \sigma_R(L) + C_\theta \cdot \sigma_\theta(L)\right]\cdot R\mathrm{d}\theta \tag{14}$$

where R denotes the resonator radius in the absence of perturbation and the two stress-optical coupling constants are defined as follows:

$$C_R = n_{\mathrm{eff}} \frac{\partial \varepsilon_L}{\partial \sigma_R} + \frac{\partial n_{\mathrm{eff}}}{\partial \sigma_R} \tag{15}$$

and

$$C_\theta = n_{\mathrm{eff}} \frac{\partial \varepsilon_L}{\partial \sigma_\theta} + \frac{\partial n_{\mathrm{eff}}}{\partial \sigma_\theta} \tag{16}$$

We note that first-principle calculations of the two stress-optical coupling constants can be challenging, since the photoelastic constants of the constituent materials are not always known. Nevertheless, these constants can be experimentally measured using a calibration sample. The calibration sample contains two sets of waveguide Fabry-Perot (F-P) cavities oriented in orthogonal directions, where each set of the F-P cavities contains a series of devices with

identical Bragg mirror designs but varying cavity lengths L_{tot}. The cavities are formed by engraving two Bragg grating reflectors on waveguides. The waveguide dimensions of the calibration sample are chosen such that they match those of the stretchable micro-ring resonator sample. The F-P cavity's resonant condition is given by:

$$2n_{\text{eff}}L_{\text{tot}} + \frac{\varphi_{\text{m}}\lambda_0}{\pi} = N\lambda_0 \tag{17}$$

where φ_{m} is the phase delay imparted upon Bragg mirror reflection in radians. The calibration sample is uniaxially bent (or stretched) along two orthogonal directions parallel to the two sets of F-P cavities. The bending (or stretching) action exerts in-plane bi-axial stresses on the F-P cavities along longitudinal and transverse directions with respect to the F-P cavity. Unlike the case of the stretchable resonators, stresses in the calibration sample resulting from uniaxial bending or stretching are spatially uniform. The resonance detuning can therefore be deduced from the F-P cavity resonant condition:

$$\frac{2n_{\text{eff}}L_{\text{tot}}}{\lambda_0} + \frac{\varphi_{\text{m}}}{\pi} = N \tag{18}$$

Taking derivative with respect to a stress component σ:

$$\frac{\partial\left(\frac{2n_{\text{eff}}L_{\text{tot}}}{\lambda_0}\right)}{\partial\sigma} + \frac{1}{\pi}\frac{\partial\varphi_{\text{m}}}{\partial\sigma} = 0 \tag{19}$$

$$\Rightarrow \frac{2n_{\text{eff}}L_{\text{tot}}}{\lambda_0}\frac{\partial\varepsilon_L}{\partial\sigma} - \frac{2n_{\text{eff}}L_{\text{tot}}}{\lambda_0^{\,2}}\frac{\partial\lambda_0}{\partial\sigma} + \frac{2L_{\text{tot}}}{\lambda_0}\frac{\partial n_{\text{eff}}}{\partial\sigma} + \frac{2L_{\text{tot}}}{\lambda_0}\frac{\partial n_{\text{eff}}}{\partial\lambda_0}\frac{\partial\lambda_0}{\partial\sigma} + \frac{1}{\pi}\frac{\partial\varphi_{\text{m}}}{\partial\sigma} = 0 \tag{20}$$

$$\Rightarrow \frac{\partial\lambda_0}{\partial\sigma} = \frac{\lambda_0}{n_{\text{g}}}\left(n_{\text{eff}}\frac{\partial\varepsilon_L}{\partial\sigma} + \frac{\partial n_{\text{eff}}}{\partial\sigma}\right) + \frac{\lambda_0^{\,2}}{2\pi n_{\text{g}}L_{\text{tot}}}\frac{\partial\varphi_{\text{m}}}{\partial\sigma} \tag{21}$$

$$\Rightarrow \frac{\partial\lambda_0}{\partial\sigma} = \frac{\lambda_0}{n_{\text{g}}}\cdot C + \frac{\lambda_0^{\,2}}{2\pi n_{\text{g}}L_{\text{tot}}}\frac{\partial\varphi_{\text{m}}}{\partial\sigma} \tag{22}$$

Eqs. 19-22 apply to both longitudinal and transverse stress components, and C represents the stress-optical coupling constant defined in Eqs. 15 and 16. When the calibration sample undergo bending or stretching, Eq. 22 yields the resonant wavelength shifts of the two orthogonal sets F-P cavity devices (labeled as set A and set B) as:

$$\mathrm{d}\lambda_{0,\text{A}} = \frac{\partial\lambda_{0,\text{A}}}{\partial\sigma_1}\cdot\sigma_1 + \frac{\partial\lambda_{0,\text{A}}}{\partial\sigma_2}\cdot\sigma_2 = \left(\frac{\lambda_{0,\text{A}}}{n_{\text{g}}}\cdot C_\theta + \frac{\lambda_{0,\text{A}}^{\,2}}{2\pi n_{\text{g}}L_{\text{tot}}}\frac{\partial\varphi_{\text{m}}}{\partial\sigma_\theta}\right)\cdot\sigma_1 + \left(\frac{\lambda_{0,\text{A}}}{n_{\text{g}}}\cdot C_R + \frac{\lambda_{0,\text{A}}^{\,2}}{2\pi n_{\text{g}}L_{\text{tot}}}\frac{\partial\varphi_{\text{m}}}{\partial\sigma_R}\right)\cdot\sigma_2 \tag{23}$$

$$\mathrm{d}\lambda_{0,\text{B}} = \frac{\partial\lambda_{0,\text{B}}}{\partial\sigma_1}\cdot\sigma_1 + \frac{\partial\lambda_{0,\text{B}}}{\partial\sigma_2}\cdot\sigma_2 = \left(\frac{\lambda_{0,\text{B}}}{n_{\text{g}}}\cdot C_R + \frac{\lambda_{0,\text{B}}^{\,2}}{2\pi n_{\text{g}}L_{\text{tot}}}\frac{\partial\varphi_{\text{m}}}{\partial\sigma_R}\right)\cdot\sigma_1 + \left(\frac{\lambda_{0,\text{B}}}{n_{\text{g}}}\cdot C_\theta + \frac{\lambda_{0,\text{B}}^{\,2}}{2\pi n_{\text{g}}L_{\text{tot}}}\frac{\partial\varphi_{\text{m}}}{\partial\sigma_\theta}\right)\cdot\sigma_2 \tag{24}$$

Since the stress-optical coupling constants C's are identical for F-P cavities of different lengths and define $\gamma = \sigma_2/\sigma_1$, the equations reduce to:

$$\frac{\mathrm{d}\lambda_{0,\text{A}}}{\sigma_1} = \frac{\lambda_{0,\text{A}}}{n_{\text{g}}}\cdot C_\theta + \frac{\lambda_{0,\text{A}}}{n_{\text{g}}}\cdot\gamma C_R + \left(\frac{\lambda_{0,\text{A}}^{\,2}}{2\pi n_{\text{g}}}\frac{\partial\varphi_{\text{m}}}{\partial\sigma_\theta} + \frac{\gamma\lambda_{0,\text{A}}^{\,2}}{2\pi n_{\text{g}}}\frac{\partial\varphi_{\text{m}}}{\partial\sigma_R}\right)\cdot\frac{1}{L_{\text{tot}}} \tag{25}$$

$$\frac{\mathrm{d}\lambda_{0,\mathrm{B}}}{\sigma_1} = \frac{\lambda_{0,\mathrm{B}}}{n_{\mathrm{g}}} \cdot C_R + \frac{\lambda_{0,\mathrm{B}}}{n_{\mathrm{g}}} \cdot \gamma C_\theta + \left(\frac{{\lambda_{0,\mathrm{B}}}^2}{2\pi n_{\mathrm{g}}} \frac{\partial \varphi_{\mathrm{m}}}{\partial \sigma_R} + \frac{\gamma {\lambda_{0,\mathrm{B}}}^2}{2\pi n_{\mathrm{g}}} \frac{\partial \varphi_{\mathrm{m}}}{\partial \sigma_\theta} \right) \cdot \frac{1}{L_{\mathrm{tot}}} \tag{26}$$

The terms marked with red color in Eqs. 25 and 26 are associated with contribution from the Bragg reflectors. Plotting the resonance shifts measured from F-P cavities of different lengths as a function of $1/L_{\mathrm{tot}}$ allows subtraction of the Bragg reflector contribution:

$$\frac{\mathrm{d}\lambda_{0,\mathrm{A}}}{\sigma_1}\left(\frac{1}{L_{\mathrm{tot}}} \to 0 \right) = \frac{\lambda_{0,\mathrm{A}}}{n_{\mathrm{g}}} \cdot C_\theta + \frac{\lambda_{0,\mathrm{A}}}{n_{\mathrm{g}}} \cdot \gamma C_R \tag{27}$$

$$\frac{d\lambda_{0,\mathrm{B}}}{\sigma_1}\left(\frac{1}{L_{tot}} \to 0 \right) = \frac{\lambda_{0,\mathrm{B}}}{n_g} \cdot C_R + \frac{\lambda_{0,\mathrm{B}}}{n_g} \cdot \gamma C_\theta \tag{28}$$

Solving the two linear equations allows extraction of the two stress-optical coupling constants C_R and C_θ. Knowledge of the stress distribution from finite element simulations thereby enables quantitative prediction of stress-induced resonant wavelength shift in a stretchable resonator by integrating Eq. 14. As an example, Supplementary Section VII presents the experimental data and detailed protocols for C_R and C_θ parameterization in our stretchable ChG/SU-8 devices.

Section VI – Coupling of shear stresses to optical modes

In this section, we prove that shear stresses have negligible influence of the optical modal properties of guided wave devices. Shear stresses can modify both the dielectric tensor of waveguide's constituent materials and the waveguide geometry. In the following we consider both effects. For the sake of convenience, we label the light propagation direction in the waveguide as *x*, and the out-of-plane direction as *z*.

In isotropic materials such as glasses and polymers, the photoelasticity tensor can be generically written as:

$$\boldsymbol{p} = \begin{bmatrix} p_{11} & p_{12} & p_{12} & 0 & 0 & 0 \\ p_{12} & p_{11} & p_{12} & 0 & 0 & 0 \\ p_{12} & p_{12} & p_{11} & 0 & 0 & 0 \\ 0 & 0 & 0 & p_{44} & 0 & 0 \\ 0 & 0 & 0 & 0 & p_{44} & 0 \\ 0 & 0 & 0 & 0 & 0 & p_{44} \end{bmatrix} \tag{29}$$

Here we follow the formalism by Chen *et al.*[2] and define the photoelasticity tensor through:

$$\Delta\boldsymbol{B} = \boldsymbol{p} \cdot \boldsymbol{S} \tag{30}$$

In Eq. 30, $\Delta\boldsymbol{B}$ is the strain-induced modification of the relative dielectric impermeability tensor $\boldsymbol{B}$ (defined as $1/\boldsymbol{\varepsilon_r}$ where $\boldsymbol{\varepsilon_r}$ is the relative permittivity tensor), and $\boldsymbol{S}$ denotes the strain tensor. Both tensors have six independent elements and thus $\boldsymbol{p}$ is a fourth order tensor represented by a 6 × 6 matrix.

If the applied strain is sufficiently small such that the material is Hookean and that the change of the dielectric constant is small, we have:

$$\Delta\boldsymbol{\varepsilon}_{\mathrm{r}} = \boldsymbol{P} \cdot \boldsymbol{T} \tag{31}$$

where $\Delta\boldsymbol{\varepsilon}_{\mathbf{r}}$ gives the relative permittivity change (which is a second order tensor) and $\boldsymbol{T}$ represents the stress tensor. The fourth order tensor $\boldsymbol{P}$ is given by:

$$\boldsymbol{P} = -\frac{\varepsilon_{\mathrm{r}}^{\,2}}{Y} \begin{bmatrix} p_{11}-2\sigma p_{12} & p_{12}-\sigma(p_{11}+p_{12}) & p_{12}-\sigma(p_{11}+p_{12}) & 0 & 0 & 0 \\ p_{12}-\sigma(p_{11}+p_{12}) & p_{11}-2\sigma p_{12} & p_{12}-\sigma(p_{11}+p_{12}) & 0 & 0 & 0 \\ p_{12}-\sigma(p_{11}+p_{12}) & p_{12}-\sigma(p_{11}+p_{12}) & p_{11}-2\sigma p_{12} & 0 & 0 & 0 \\ 0 & 0 & 0 & \frac{p_{44}Y}{\mu} & 0 & 0 \\ 0 & 0 & 0 & 0 & \frac{p_{44}Y}{\mu} & 0 \\ 0 & 0 & 0 & 0 & 0 & \frac{p_{44}Y}{\mu} \end{bmatrix} \tag{32}$$

In Eq. 32, the unbolded ε_{r} is the relative permittivity (a scalar number for isotropic solids), Y and μ are the Young' modulus and shear modulus, respectively, and σ denotes the Poisson ratio.

Since the change of the dielectric constant is small, optical mode variation due to the stress-induced permittivity modification can be calculated using the classical perturbation theory. For a waveguide device, the propagation constant change $\Delta\beta$ is expressed as[3]:

$$\Delta\beta = \frac{\omega\varepsilon_0}{2} \cdot \frac{\iint \mathrm{d}^2 r \cdot \left(\Delta\boldsymbol{\varepsilon}_{\mathrm{r}} \vec{E}\right) \cdot \vec{E}^*}{\iint \mathrm{d}^2 r \cdot \mathrm{Re}\left(\vec{E} \times \vec{H}^*\right) \cdot \hat{x}} \tag{33}$$

where $\vec{E}$ and $\vec{H}$ are the unperturbed mode, ω is the angular frequency of light, and ε_0 gives the vacuum permittivity.

Eqs. 31 and 32 specify that shear stresses only affect the off-diagonal terms in the permittivity tensor. Based on Eq. 33, the perturbative effects scales with the term $\left(\Delta\boldsymbol{\varepsilon}_{\mathrm{r}} E\right) \cdot E^*$, which vanishes for the off-diagonal permittivity tensor terms.

Next, we investigate the geometric effects imposed by shear stresses. In a thin-membrane flexible photonic device with free surfaces, only the in-plane shear stress component T_{xy} is present. Modal perturbation resulting from the shear deformation caused by T_{xy} is most conveniently evaluated by invoking the perturbation theory involving shifting material boundaries[4]:

$$\Delta\omega = -\frac{\omega}{2} \cdot \frac{\iint \mathrm{d}^2 r \cdot \left[\left(\varepsilon_1 - \varepsilon_2\right) \left|E_{//}\left(r\right)\right|^2 - \left(\frac{1}{\varepsilon_1} - \frac{1}{\varepsilon_2}\right) \left|\varepsilon E_{\perp}\left(r\right)\right|^2 \right] \cdot \Delta h}{\iiint \mathrm{d}^3 r \cdot \varepsilon\left(r\right) \left|E\left(r\right)\right|^2} \tag{34}$$

where ε_1 and ε_2 represent the permittivity on two sides of the shifting boundary, $E_{//}$ and $E_{\perp}$ are the modal electric field parallel and perpendicular to the boundary respectively, and Δh denotes displacement of the boundary. In a device exhibiting mirror symmetry with respect to the x or y axis, the optical mode must also be symmetric or anti-symmetric about the same axis. The terms containing $|E|^2$ thus obey mirror symmetry. Since the shear stress T_{xy} generates an anti-symmetric displacement field about the axis of symmetry, it is straightforward to deduce from Eq. 34 that perturbative effects due to shifted boundaries on two sides of the symmetric device structure cancel out each other. We therefore conclude that shear stresses have a negligible contribution to optical mode perturbation.

Section VII – Extracting C_R and C_θ from calibration sample measurements

A calibration sample containing two set of waveguide F-P cavities with orthogonal orientations were fabricated on flexible substrates following protocols employed by our previously demonstrated foldable photonic devices[5]. Each set includes four devices with varying cavity length L_{tot}. The sample was then bent to different radii while the resonant wavelengths of the F-P cavities were monitored (Fig. S7a). Orientations of the two sets of devices (labeled as A and B) with respect to the bending direction are illustrated in Fig. 4a. As an example, Figures S5 presents the evolution of transmission spectra of devices when they were bent to different radii, and Fig. S6 summarizes the F-P cavity resonance peak detuning for both sets of devices as functions of local stresses exerted on the devices during bending, which were modeled using FEM simulations based on given bending radii of the sample.

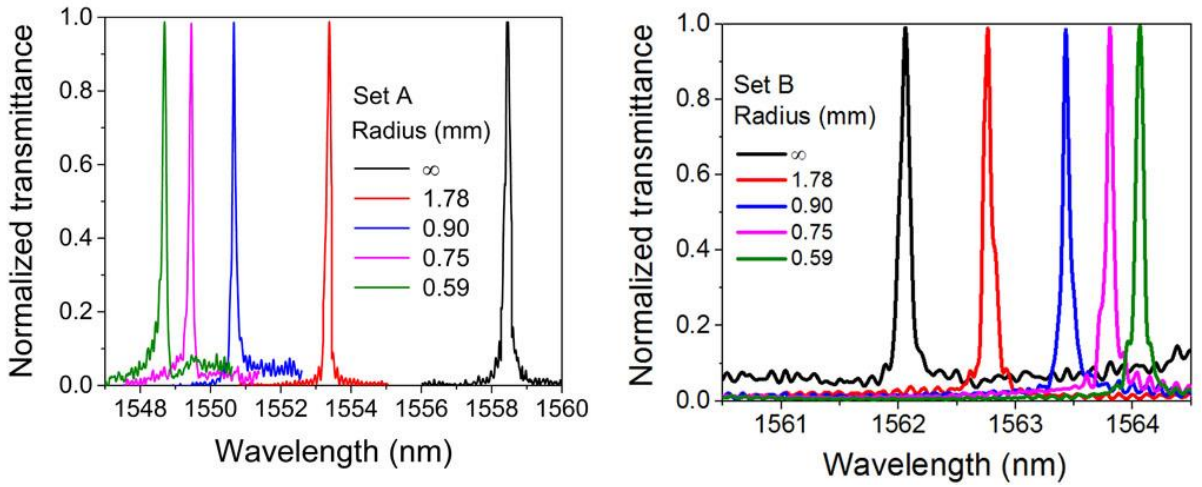

Figure S5. Exemplary transmission spectra of F-P cavity devices in (left) set A and (right) set B, showing resonance spectral detuning due to bending deformation.

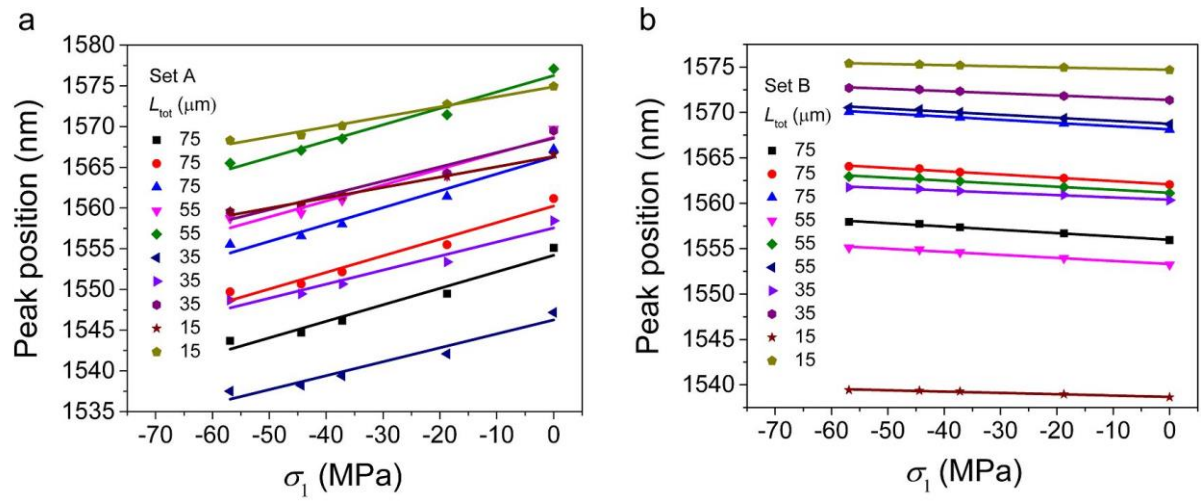

Figure S6. Resonant peak positions as functions of local stress for device (a) set A and (b) set B.

In the next step, the slopes $d\lambda/\sigma_1$ were computed from Fig. S6 for all the curves, averaged for each cavity length L_{tot}, and plotted against $1/L_{tot}$ for each device set as shown in Fig. S7. Intercepts of the lines in Fig. S7b with the vertical axis $1/L_{tot} = 0$ correspond to $\frac{d\lambda_{0,A}}{\sigma_1}\left(\frac{1}{L_{tot}} \to 0\right)$ and $\frac{d\lambda_{0,B}}{\sigma_1}\left(\frac{1}{L_{tot}} \to 0\right)$. C_R and C_θ are then solved by combining Eqs. 27 and 28 in Supplementary Section V. Our measurements yield $C_R = (1.32 \pm 0.08) \times 10^{-10}$ Pa^{-1} and $C_\theta = (3.42 \pm 0.08) \times 10^{-10}$ Pa^{-1}. The error bars associated with these stress-optical coupling constants are quantitatively evaluated in Supplementary Section IX.

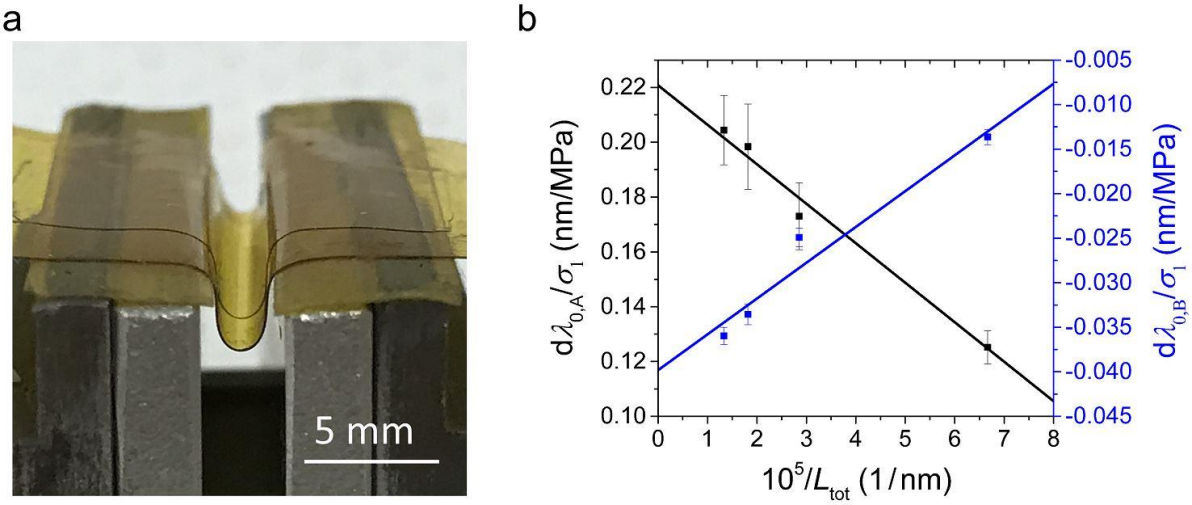

Figure S7. (a) Photo of a calibration sample under test; (b) $d\lambda_0/\sigma_1$ obtained from Fig. S6 for device set A (black) and B (blue). The dots are data calculated from Fig. S6 and the lines are linear fits.

Section VIII – Quantification of strain-optical coupling contributions from geometric and photoelastic terms

Here we consider two waveguide configurations under stress as sketched in the insets of Figures 4f and 4g. Since in-plane normal stresses are the only stress components affecting the optical modal characteristics according to Supplementary Section VI, linear combinations of the two cases cover all possible scenarios of stressed flexible membrane waveguide devices.

For the axially stressed case shown in Fig. 4f inset, the stress-induced resonance drift is:

$$\mathrm{d}\lambda_0 = \frac{\lambda_0}{n_\mathrm{g}} \cdot C_\theta \sigma \tag{35}$$

Similarly, the resonance shift when stress is applied in the transverse direction (Fig. 4g) is:

$$\mathrm{d}\lambda_0 = \frac{\lambda_0}{n_\mathrm{g}} \cdot C_R \sigma \tag{36}$$

For a given stress magnitude, the device geometric deformation (length change and waveguide cross-section modification) was calculated through FEM mechanical modeling. The waveguide cross-section modifications were then fed into a waveguide mode solver (MODE Solutions, Lumerical Solutions, Inc.) to compute the effective index perturbation. Finally, the photoelastic contributions were quantified by subtracting the two geometric terms from the total resonance shift given by Eqs. 35 and 36.

Table S2 compiles the calculation results. In the table, the stress value refers to stress in the SU-8 cladding. Since the final results are normalized, we fix the stress at 1 MPa for this calculation. Figures 4f and 4g were plotted using the normalized data in the last column.

Table S2. Quantifying contributions from geometric and photoelastic terms to resonance shift

	Strain-Optical Coupling Mechanism	Contribution to resonance shift (at 1 MPa stress)	Normalized contribution
Set A	Total	0.241	1
	Cross-section deformation	-0.056	-0.23
	Length change	0.592	2.45
	Photoelasticity	-0.295	-1.22
Set B	Total	-0.093	-1
	Cross-section deformation	0.029	0.31
	Length change	-0.050	-0.53
	Photoelasticity	-0.072	-0.78

Section IX – Error analysis of stress-optical coefficient measurement

This section discusses how the errors of initial experiment results propagate to the final calculated stress-optical coupling coefficients. Through solving the two linear equations Eq. 27 and Eq. 28, the stress-optic coupling constants C_θ and C_R can be expressed as:

$$\frac{\lambda_0}{n_\mathrm{g}} C_\theta = \frac{\gamma \frac{\mathrm{d}\lambda_{0,\mathrm{B}}}{\sigma_1}\left(\frac{1}{L_\mathrm{tot}} \to 0\right) - \frac{\mathrm{d}\lambda_{0,\mathrm{A}}}{\sigma_1}\left(\frac{1}{L_\mathrm{tot}} \to 0\right)}{\gamma^2 - 1} \tag{37}$$

$$\frac{\lambda_0}{n_\mathrm{g}} C_R = \frac{\gamma \frac{\mathrm{d}\lambda_{0,\mathrm{A}}}{\sigma_1}\left(\frac{1}{L_\mathrm{tot}} \to 0\right) - \frac{\mathrm{d}\lambda_{0,\mathrm{B}}}{\sigma_1}\left(\frac{1}{L_\mathrm{tot}} \to 0\right)}{\gamma^2 - 1} \tag{38}$$

According to the standard addition and subtraction rules of values with error, the uncertainty (standard deviation (S.D.)) of C_θ and C_R are:

$$S_\theta = S_R = \sqrt{S_\mathrm{A}^2 + S_\mathrm{B}^2} \tag{39}$$

where S_θ, S_R, S_A , and S_B are the S.D. of C_θ, C_R, $\frac{\mathrm{d}\lambda_{0,\mathrm{A}}}{\sigma_1}\left(\frac{1}{L_\mathrm{tot}} \to 0\right)$, and $\frac{\mathrm{d}\lambda_{0,\mathrm{B}}}{\sigma_1}\left(\frac{1}{L_\mathrm{tot}} \to 0\right)$, respectively. $\frac{\mathrm{d}\lambda_{0,\mathrm{A}}}{\sigma_1}\left(\frac{1}{L_\mathrm{tot}} \to 0\right)$ and $\frac{\mathrm{d}\lambda_{0,\mathrm{B}}}{\sigma_1}\left(\frac{1}{L_\mathrm{tot}} \to 0\right)$ are the intercepts of the fitted lines of $\frac{\mathrm{d}\lambda_{0,\mathrm{A}}}{\sigma_1}$ *vs.* $\frac{1}{L}$, $\frac{\mathrm{d}\lambda_{0,\mathrm{B}}}{\sigma_1}$ *vs.* $\frac{1}{L}$ shown in Fig. S7b, in which the value and error of each data point $\mathrm{d}\lambda/\sigma_1$ was calculated from the combination of multiple averaged linear fitting slopes and their errors are shown in Fig. S6.

To understand how the error propagates, first let's briefly review the standard deviations of line slope and intercept in a linear fitting. Assuming that we have a set of data points whose coordinates are given by x_1, x_2,…, x_n and y_1, y_2,…, y_n, and the x's and y's have a best linear fit expressed as $y = kx + m$, the fitting error (S.D.) of slope k and intercept m can be evaluated via:

$$S_k = S\sqrt{\frac{n}{\left(n\sum x_i^2\right) - \left(\sum x_i\right)^2}} \tag{40}$$

$$S_m = S\sqrt{\frac{\sum x_i^2}{\left(n\sum x_i^2\right) - \left(\sum x_i\right)^2}} \tag{41}$$

$$S = \sqrt{\frac{1}{n-2}\sum_{i=1}^{n}\left[y_i - \left(m + kx_i\right)\right]^2} \tag{42}$$

However, if we want to calculate the fitting parameters (slopes and intercepts) and their errors with more than one set of data points, the following equation should be used to combine multiple averaged data points and their errors.

$$S_\mathrm{ab} = \sqrt{\frac{N_\mathrm{a}}{N} S_\mathrm{a}^2 + \frac{N_\mathrm{b}}{N} S_\mathrm{b}^2 + \frac{n_\mathrm{a} n_\mathrm{b}}{nN}(\bar{a} - \bar{b})^2}\ , \text{where} \tag{43}$$

$$n = n_\mathrm{a} + n_\mathrm{b} \tag{44}$$

$$N = n(n-1) \tag{45}$$

$$N_a = n_a(n_a - 1) \tag{46}$$

$$N_b = n_b(n_b - 1) \tag{47}$$

Here S_a, S_b, and S_{ab} are the standard deviations of data set a, data set b, and the combined data set of a and b; n_a and n_b are the number of data points in data sets a and b; and $\bar{a}$ *and* $\bar{b}$ are the average value of data sets a and b. Repeat the above protocols to obtain S.D. for three or more combined data sets if needed.

To analyze the error propagation in our measurement, we have used the linear fitting function in the Origin software to directly obtain the value and error of fitted slopes $d\lambda/\sigma_1$ for each data set in Fig. S6. The details numbers are summarized in Table S3.

Table S3. Summary of the values and errors of fitted slopes $d\lambda/\sigma_1$ in Fig. S6

Set A			**Set B**		
***L* (μm)**	**$d\lambda/\sigma_1$ (nm MPa^{-1})**	**S.D. (nm MPa^{-1})**	***L* (μm)**	**$d\lambda/\sigma_1$ (nm MPa^{-1})**	**S.D. (nm MPa^{-1})**
75	0.20261	0.02322	75	-0.03647	0.00203
75	0.20371	0.02379	75	-0.03628	0.00186
75	0.20691	0.02411	75	-0.03519	0.00146
55	0.19546	0.02625	55	-0.03369	0.00221
55	0.20131	0.0199	55	-0.03353	0.00224
35	0.17111	0.02305	55	-0.03344	0.00205
35	0.17249	0.02231	35	-0.02543	0.00165
35	0.17542	0.02302	35	-0.02438	0.00139
15	0.1268	0.00915	15	-0.01454	0.00157
15	0.12347	0.00895	15	-0.01275	0.00065

To combine the results of multiple samples with the same F-P cavity length, Eqs. 43-47 were used to calculate the final values and errors of $d\lambda/\sigma_1$ for samples with different cavity lengths. The calculated numbers as well as the fitted intercepts using those numbers in Origin software (Fig. S7) are tabulated in Table S4.

Table S4. Summary of the values and errors of fitted slopes $d\lambda/\sigma_1$ from combining the results of multiples samples in Fig. S6 as well as the linear fitting results in Fig. S7

Set A				
***L* (μm)**	**$d\lambda/\sigma_1$ (nm/MPa)**	**S.D. (nm/MPa)**	**Fitted intercept** $\frac{d\lambda_{0,A}}{\sigma_1}\left(\frac{1}{L_{tot}} \to 0\right)$	
75	0.20441	0.012683	**Value (nm MPa^{-1})**	**S.D. (S_A) (nm MPa^{-1})**
55	0.198385	0.015559	**0.2208**	**0.00507**
35	0.173007	0.012194		
15	0.125135	0.006059		

Set B				
L (μm)	**$d\lambda/\sigma_1$ (nm MPa^{-1})**	**S.D. (nm MPa^{-1})**	**Fitted intercept** $\frac{d\lambda_{0,B}}{\sigma_1}\left(\frac{1}{L_{tot}}\to 0\right)$	
75	-0.03598	0.000973	**Value (nm MPa^{-1})**	**S.D. (S_B) (nm MPa^{-1})**
55	-0.03355	0.001159	**-0.03982**	**0.00249**
35	-0.02491	0.001032		
15	-0.01365	0.000855		

By substituting the values of $\frac{d\lambda_{0,A}}{\sigma_1}\left(\frac{1}{L_{tot}}\to 0\right)$ and $\frac{d\lambda_{0,B}}{\sigma_1}\left(\frac{1}{L_{tot}}\to 0\right)$ in Table S4 into Eq. 37 and Eq. 38 (where Poisson ratio of SU-8 is taken as 0.22), we get:

$$\frac{\lambda}{n_g}C_\theta = 0.241236 \pm 0.005648 \text{ (nm MPa}^{-1}\text{)} \tag{48}$$

$$\frac{\lambda}{n_g}C_R = -0.092892 \pm 0.005648 \text{ (nm MPa}^{-1}\text{)} \tag{49}$$

$$S_\theta = S_R = \sqrt{S_A^2 + S_B^2} = \sqrt{0.00507^2 + 0.00249^2} = 0.005648 \text{ (nm MPa}^{-1}\text{)} \tag{50}$$

In our experiment, group index n_g of the ChG/SU-8 waveguide is calculated to be 2.2 from our mode solver and the device test wavelength λ_0 is set around 1550 nm, so the stress-optic coupling coefficients are:

$$C_\theta = (3.42 \pm 0.08) \times 10^{-10} \text{ (Pa}^{-1}\text{)} \tag{51}$$

$$C_R = (-1.32 \pm 0.08) \times 10^{-10} \text{ (Pa}^{-1}\text{)} \tag{52}$$

We note that here the two coefficients are defined with respect to the stresses in SU-8. The actual stresses in the $Ge_{23}Sb_7S_{70}$ chalcogenide glass is about 8 times higher given its larger elastic modulus. Therefore, the measurement accuracy for stress-optic coefficients referenced to stresses in the glass material is about 10^{-12} Pa^{-1}.

References

1 SU-8 Permanent Photoresists. http://www.microchem.com/pdf/SU-8-table-of-properties.pdf, *retrieved on 05/01/2017*.

2 Chen CL. *Foundations for guided-wave optics*. John Wiley & Sons 2006.

3 Kogelnik H. in *Guided-wave optoelectronics*. Springer 1988; 7-88.

4 Johnson SG, Ibanescu M, Skorobogatiy MA, Weisberg O, Joannopoulos JD. Perturbation theory for Maxwell's equations with shifting material boundaries. *Physical Review E* 2002; **65**: 066611.

5 Li L, Lin HT, Qiao ST, Zou Y, Danto S *et al*. Integrated flexible chalcogenide glass photonic devices. *Nat Photonics* 2014; **8**: 643-649.